

# GLOBAL THREE-DIMENSIONAL MHD SIMULATIONS OF GALACTIC GASEOUS DISKS: I. AMPLIFICATION OF MEAN MAGNETIC FIELDS IN AXISYMMETRIC GRAVITATIONAL POTENTIAL

Hiromitsu Nishikori<sup>1</sup>

*Graduate School of Science and Technology, Chiba University, 1-33, Yayoi-cho, Inage-ku,  
Chiba 263-8522, Japan*

[nisikori@astro.s.chiba-u.ac.jp](mailto:nisikori@astro.s.chiba-u.ac.jp)

Mami Machida<sup>2</sup>

*National Astronomical Observatory of Japan, 2-21-1, Osawa, Mitaka, Tokyo 181-8588,  
Japan*

and

Ryoji Matsumoto<sup>3</sup>

*Department of Physics, Faculty of Science, Chiba University, 1-33, Yayoi-cho, Inage-ku,  
Chiba 263-8522, Japan*

## ABSTRACT

We carried out global three-dimensional resistive magnetohydrodynamic simulations of galactic gaseous disks to investigate how the galactic magnetic fields are amplified and maintained. We adopt a steady axisymmetric gravitational potential given by Miyamoto & Nagai (1975) and Miyamoto, Satoh & Ohashi (1980). As the initial condition, we assume a warm ( $T \sim 10^5$  K) rotating gas torus centered at  $\varpi = 10$  kpc threaded by weak azimuthal magnetic fields. Numerical results indicate that in differentially rotating galactic gaseous disks, magnetic fields are amplified due to magneto-rotational instability and magnetic turbulence develops. After the amplification of magnetic energy saturates, the disk stays in a quasi-steady state. The mean azimuthal magnetic field increases with time and shows reversals with period of 1Gyr (2Gyr for a full cycle). The amplitude of  $B_\varphi$  near the equatorial plane is  $B_\varphi \sim 1.5\mu$  G at  $\varpi = 5$  kpc. The magnetic fields show large fluctuations whose standard deviation is comparable

to the mean field. The mean azimuthal magnetic field in the disk corona has direction opposite to the mean magnetic field inside the disk. The mass accretion rate driven by the Maxwell stress is  $\sim 10^{-3}M_{\odot}/\text{yr}$  at  $\varpi = 2.5 \text{ kpc}$  when the mass of the initial torus is  $\sim 5 \times 10^8 M_{\odot}$ . When we adopt an absorbing boundary condition at  $r = 0.8 \text{ kpc}$ , the rotation curve obtained by numerical simulations almost coincides with the rotation curve of the stars and the dark matter. Thus even when magnetic fields are not negligible for gas dynamics of a spiral galaxy, galactic gravitational potential can be derived from observation of rotation curves using gas component of the disk.

*Subject headings:* galaxies: spiral—ISM: magnetic fields—MHD

## 1. INTRODUCTION

Spiral galaxies have magnetic fields. In our Galaxy, the average magnetic field strength is a few  $\mu\text{G}$ . (e.g., Sofue, Fujimoto & Wielebinski 1986; Beck et al. 1996). These magnetic fields have been explained by the dynamo action operating in galactic gas disks (e.g., Parker 1971). In conventional theory of galactic dynamos, the following induction equation is solved;

$$\frac{\partial \bar{\mathbf{B}}}{\partial t} = \nabla \times (\mathbf{v} \times \bar{\mathbf{B}}) + \eta \nabla^2 \bar{\mathbf{B}} + \nabla \times (\alpha \bar{\mathbf{B}}), \quad (1)$$

where  $\eta$  denotes the turbulent magnetic diffusivity,  $\mathbf{v}$  is the mean velocity, and  $\bar{\mathbf{B}}$  is the mean magnetic field. The last term on the right hand side of equation (1) is the dynamo term which represents the re-generation of mean magnetic fields ( $\alpha$  effect). When velocity fields  $\mathbf{v}$  are given, equation (1) is linear with  $\bar{\mathbf{B}}$ . It can be solved with appropriate boundary conditions. This approach is referred to as the *kinematic dynamo*. The effects of nonlinearities such as the quenching of the  $\alpha$ -effect for strong magnetic fields and the loss of magnetic flux due to the magnetic buoyancy have also been studied in the framework of the kinematic dynamo theory (e.g., Schmitt & Schüssler 1989; Brandenburg et al. 1989, 1992).

In 1990s, it became clear that nonlinear dynamical processes are essential for the evolution of magnetic fields in differentially rotating disks. Balbus & Hawley (1991) showed that in the presence of weak magnetic fields, differentially rotating gas disks subject to the robust magneto-rotational instability (MRI). This instability is caused by the back-reaction of magnetic fields to the fluid motion. Thus, in order to study the evolution of magnetic fields in differentially rotating disks, we should solve the momentum equation including Lorentz force simultaneously with the induction equation. This approach is called *dynamical dynamo*. The developments of computational magnetohydrodynamics (MHD) enabled us to study this dynamical dynamo process by direct three-dimensional (3D) global simulations.

In the context of accretion disks, the nonlinear growth of MRI was first studied by local 3D MHD simulations (e.g., Hawley, Gammie & Balbus 1995; Matsumoto & Tajima 1995; Brandenburg et al. 1995). They showed that MRI drives magnetic turbulence in accretion disks and amplifies magnetic fields. Subsequently, global 3D MHD simulations of initially weakly magnetized rotating torus were carried out (e.g., Matsumoto 1999; Hawley 2000; Machida, Hayashi & Matsumoto 2000). They showed that the magnetic field amplification saturates when  $\beta = P_{\text{gas}}/P_{\text{mag}} \sim 10$ . The magnetic fields maintained in the quasi-steady state are mainly toroidal but have turbulent poloidal components. They also showed that in the innermost region of black hole accretion disks where radial infall of disk gas becomes important, spiral magnetic fields which accompany radial field reversals are created (e.g., Machida & Matsumoto 2003).

In numerical studies of accretion disks, the gravitational field is assumed to be that of the central point mass. It is straightforward to extend this gravitational potential to more general potentials such as those of spiral galaxies. Since the galactic gaseous disk is also a differentially rotating disk, it subjects to the MRI. The growth of MRI and generation of MHD turbulence in galactic HI disks were discussed by Sellwood & Balbus (1999). Kim, Ostriker & Stone (2003) carried out three-dimensional local MHD simulations of galactic gaseous disks and showed that MRI drives interstellar turbulence and helps forming the giant molecular clouds. The coupling of the thermal instability and MRI in the interstellar space has been studied by Piontek & Ostriker (2004).

Dziourkevitch & Elstner (2003) reported the results of global three-dimensional MHD simulations of the galactic gaseous disks including the dynamo  $\alpha$  term. More recently, Dziourkevitch, Elstner & Rüdiger (2004) carried out global three-dimensional MHD simulations of galactic gaseous disks without assuming the dynamo  $\alpha$  term starting from vertical magnetic fields and showed that mean magnetic fields and interstellar turbulence are generated. However, their simulation area was limited to 5kpc in the radial direction and 1kpc in the vertical direction. Kitchatinov, & Rüdiger (2004) carried out linear but global analysis for MRI in a disk geometry and showed that MRI can amplify very weak seed magnetic fields in proto-galaxies.

In this paper, we report the results of global 3D MHD simulations of galactic gaseous disks by using the axisymmetric gravitational potential created by stars and the dark matter. We solve the nonlinear MHD equations without introducing the phenomenological dynamo  $\alpha$  parameter. The initial magnetic field is assumed to be toroidal. This initial condition enables us to start the simulation without much disturbing the interface between the disk and the disk corona. When we start from vertical magnetic fields, efficient angular momentum loss near the surface of the initial torus drives an avalanche-like surface accretion, which

deforms magnetic field lines into an hourglass shape and produces magnetocentrifugally driven outflows (e.g., Matsumoto et al. 1996). For simplicity we neglect the multi-phase nature of galactic gaseous disk, non-axisymmetric spiral gravitational potential, self gravity and supernova explosions. These processes will be incorporated in subsequent papers.

In section 2, we present numerical methods. Numerical results are given in section 3. Section 4 is devoted for summary and discussion.

## 2. NUMERICAL METHODS

### 2.1. Basic Equations

The basic equations we solve are resistive MHD equations,

$$\frac{\partial \rho}{\partial t} + \nabla \cdot (\rho \mathbf{v}) = 0, \quad (2)$$

$$\rho \left[ \frac{\partial \mathbf{v}}{\partial t} + (\mathbf{v} \cdot \nabla) \mathbf{v} \right] = -\nabla P + \frac{1}{4\pi} (\nabla \times \mathbf{B}) \times \mathbf{B} - \rho \nabla \phi, \quad (3)$$

$$\frac{\partial \mathbf{B}}{\partial t} = \nabla \times (\mathbf{v} \times \mathbf{B} - \eta \nabla \times \mathbf{B}), \quad (4)$$

$$\begin{aligned} \frac{\partial}{\partial t} \left( \frac{1}{2} \rho v^2 + \frac{B^2}{8\pi} + \frac{P}{\gamma - 1} \right) \\ + \nabla \cdot \left[ \left( \frac{1}{2} \rho \mathbf{v}^2 + \frac{\gamma P}{\gamma - 1} \right) \mathbf{v} + \frac{c}{4\pi} \mathbf{E} \times \mathbf{B} \right] \\ = -\rho \mathbf{v} \nabla \phi. \end{aligned} \quad (5)$$

In these equations,  $\rho$ ,  $p$ ,  $\mathbf{B}$ ,  $\mathbf{v}$ ,  $\phi$  and  $\gamma$  are the density, pressure, magnetic fields, velocity, gravitational potential and the specific heat ratio, respectively. The electric field  $\mathbf{E}$  is related to the magnetic field  $\mathbf{B}$  by  $\mathbf{E} = (-\mathbf{v} \times \mathbf{B} + \eta \nabla \times \mathbf{B})/c$ . We assume the anomalous resistivity  $\eta$

$$\eta = \begin{cases} \eta_0 (v_d/v_c - 1)^2, & (\text{when } v_d > v_c), \\ 0, & (\text{when } v_d < v_c), \end{cases}$$

where  $v_d = j/\rho$  is the electron-ion drift velocity and  $v_c$  is the critical velocity above which anomalous resistivity sets in ( Yokoyama & Shibata 1994).

We adopted cylindrical coordinates  $(\varpi, \varphi, z)$ . For normalization, we take the unit radius  $\varpi_0 = 1$  kpc, and unit velocity  $v_0 = 255$  km/s. The unit time is  $t_0 = \varpi_0/v_0 = 3.8 \times 10^6$  years. For specific heat ratio and resistivity, we adopt  $\gamma = 5/3$  and  $\eta_0 = 0.01v_0\varpi_0$ , respectively.

## 2.2. Initial Condition

As the initial density distribution, we assume a rotating equilibrium torus threaded by azimuthal magnetic fields embedded in the isothermal, non-rotating, spherical hot halo (Okada, Fukue & Matsumoto 1989). We assume that the gas torus has constant specific angular momentum  $L$  and assume polytropic equation of state,  $P = K\rho^\gamma$  where  $K$  is a constant. This initial condition simulates the situation that after a spiral galaxy is formed, the interstellar gas is supplied either by accretion of intergalactic gas which has some specific angular momentum or by supernova explosions following bursts of star formation inside the galaxy at some radius. As we shall show later, the angular momentum distribution of the gas settles into that determined by the galactic gravitational potential. Thus, the final distribution of density and angular momentum is not sensitive to the initial distribution.

We assume that the Alfvén speed  $v_A$  is a function of  $\varpi B_\varphi$ ,

$$v_A^2 \equiv \frac{B_\varphi^2}{4\pi\rho} = \frac{(4\pi\mathcal{H})^{1/\mu}}{4\pi} (\varpi B_\varphi)^{2(\mu-1)/\mu}, \quad (6)$$

where  $B_\varphi$  is the toroidal magnetic field and  $\mathcal{H}$  and  $\mu$  are constants. We take  $\mu = \gamma$ . Using these assumptions, we can integrate the equation of motion into the potential form,

$$\begin{aligned} \Psi(\varpi, z) &= \phi + \frac{L^2}{2\varpi^2} + \frac{1}{\gamma-1} v_s^2 + \frac{\gamma}{2(\gamma-1)} v_A^2 = \Psi_b \\ &= \text{constant}, \end{aligned} \quad (7)$$

where  $v_s = (\gamma P/\rho)^{1/2}$  is the sound speed and  $\Psi_b = \Psi(\varpi_b, 0)$ . We take the reference radius  $\varpi_b$  at the radius of the density maximum of the torus. We adopt  $\varpi_b = 10$  kpc and set  $\rho(\varpi_b, 0) = \rho_b$ . Using equation (7), we obtain the density distribution

$$\rho = \rho_b \left[ \frac{\max\{\Psi_b - \phi(\varpi, z) - L^2/(2\varpi^2), 0\}}{K\{\gamma/(\gamma-1)\} \left(1 + \beta_b^{-1} \varpi^{2(\gamma-1)} / \varpi_b^{2(\gamma-1)}\right)} \right]^{1/(\gamma-1)}, \quad (8)$$

where  $\beta_b = (2K/\mathcal{H})/\varpi_b^{2(\gamma-1)}$  is the ratio of gas pressure to magnetic pressure at  $(\varpi, z) = (\varpi_b, 0)$ . The thermal energy of the torus is parameterized by

$$E_{th} = \frac{c_{sb}^2}{\gamma v_0^2} = 0.05, \quad (9)$$

where  $c_{sb}$  is the sound speed at  $(\varpi, z) = (\varpi_b, 0)$ . This sound speed corresponds to the temperature  $T_b \sim 2 \times 10^5$  K. This means that we assume a warm torus as the initial condition. For unit density, we take  $\rho_b = 3 \times 10^{-25}$  g/cm<sup>3</sup>. The initial gas pressure at  $(\varpi, z) = (\varpi_b, 0)$  is

$$\begin{aligned} P_b &= P(\varpi_b, 0) = \frac{1}{\gamma} \rho_b c_{sb}^2 \\ &= 10^{-11} \left( \frac{\rho_b}{3 \times 10^{-25} \text{ g/cm}^3} \right) \left( \frac{T_b}{2 \times 10^5 \text{ K}} \right) \text{ dyne/cm}^2. \end{aligned} \quad (10)$$

The density of the corona  $\rho_c$  is given by

$$\rho_c = 10^{-4} \rho_b \exp \left[ -\frac{\gamma}{c_{sc}^2} (\phi - \phi_b) \right], \quad (11)$$

where  $c_{sc}$  is the sound speed in the corona and  $\phi_b$  is the gravitational potential at  $(\varpi, z) = (\varpi_b, 0)$ . We take the characteristic coronal pressure  $P_c = \rho_c c_{sc}^2 \sim 10^{-4} \rho_b c_{sc}^2 = 3 \times 10^{-3} P_b$ .

As the gravitational potential  $\phi$ , we adopted a model of our galaxy given by Miyamoto & Nagai (1975) and Miyamoto, Satoh & Ohashi (1980). They assumed centrifugal balance only in the galactic plane. To reproduce the galactic rotation curve, three different sets of parameters  $(a_1, b_1, M_1)$ ,  $(a_2, b_2, M_2)$ ,  $(a_3, b_3, M_3)$  are introduced in the gravitational potential as follows,

$$\phi(\varpi, z) = \sum_{i=1}^3 \frac{GM_i}{[\varpi^2 + \{a_i + (z^2 + b_i^2)^{0.5}\}^2]^{0.5}}. \quad (12)$$

Here  $i = 1$  and  $2$  take into account the gravitational field by bulge and disk stars, respectively. The third component  $i = 3$  is the contribution by dark matter. In this equation, the constants  $a_i$ ,  $b_i$  and  $M_i$  have dimension of length and mass, respectively, and  $G$  is the gravitational constant. This potential is axisymmetric. The values of the constants are given in Table 1. Model I and II are models without dark matter and model III-VII include the dark matter.

Figure 1 shows the isocontours of the gravitational potential for model I. Figure 2 shows the isocontours of the initial density and toroidal magnetic field for model I.

### 2.3. Simulation Code

We solved the MHD equations by using a three-dimensional MHD code based on a modified Lax-Wendroff method ( Rubin & Burstein 1967) with artificial viscosity ( Richtmyer & Morton 1967). This code was originally developed to carry out two-dimensional axisymmetric global MHD simulations of jet formation from accretion disks (e.g., Shibata & Uchida

1985; Matsumoto et al. 1996; Hayashi, Shibata & Matsumoto 1996). The MHD code was extended to three-dimensions and has been used to carry out global three-dimensional MHD simulations of accretion disks (Machida et al. 2000; Machida & Matsumoto 2003; Kato, Mineshige & Shibata 2004).

#### 2.4. Simulation Region and Boundary Conditions

The number of mesh points is  $(N_{\varpi}, N_{\varphi}, N_z) = (250, 64, 319)$  for model I-IV. The grid size is  $\Delta\varpi = 0.05$ ,  $\Delta z = 0.01$  for  $0 \leq \varpi < 6.0$ ,  $0 \leq z < 2.0$ , and otherwise increases with  $\varpi$  and  $z$  as  $\Delta z_{k+1} = 1.05\Delta z_k$ . We used this nonuniform mesh to concentrate meshes near the galactic plane and near the central region. The size of the simulation box is  $0 \text{ kpc} < \varpi < 56 \text{ kpc}$ , and  $0 \text{ kpc} < z < 10 \text{ kpc}$ . We used this large simulation box in order to simulate the buoyant rise of magnetic flux into the galactic corona and to reduce the effects of the outer boundary condition.

We imposed free boundary conditions at  $\varpi = 56 \text{ kpc}$  and  $z = 10 \text{ kpc}$  where waves can be transmitted. For azimuthal direction, we include full circle ( $0 \leq \varphi < 2\pi$ ) for models I-IV. We carried out full circle simulations because we are interested in the formation of large-scale mean magnetic fields. We should note that the amplitude of modes with low azimuthal mode numbers ( $m = 1$  or  $m = 2$ ) are often large in global simulations of accretion disks (e.g., Machida & Matsumoto 2003). In order to study the effects of the azimuthal resolution and the azimuthal size of the simulation region, we carried out simulations for model V, VI and VII, in which the azimuthal simulation region is limited to  $0 \leq \varphi < \pi/2$ . Periodic boundary conditions are imposed in the azimuthal direction. The other parameters are the same as those for model III (Table 2).

We assume symmetric boundary condition at the equatorial plane  $z = 0$  and simulated only the upper half space. The physical quantities at rotation axis ( $\varpi = 0$ ) are computed by averaging those at the mesh point next to the axis. In models I and III-VII, we imposed absorbing boundary condition at  $r = (\varpi^2 + z^2)^{1/2} = r_{in} = 0.8 \text{ kpc}$ . We introduce a damping layer inside  $r = r_{in}$ . In this layer, the deviation of physical quantity  $q$  from initial value  $q_0$  is reduced after each time step with a damping rate  $a$ ,

$$q' = q - a(q - q_0). \quad (13)$$

Here we take

$$a = 0.1 \left( 1.0 - \tanh \frac{r - 0.8 + 5\Delta\varpi}{2\Delta\varpi} \right). \quad (14)$$

This damping layer serves as the non-reflecting boundary which absorbs accreting mass and waves propagating into  $r = 0.8$ . This boundary condition is adopted in our standard model

because the gas accreted to the central region of the galaxy will be converted to stars or absorbed by the central massive black hole. In model II, we imposed no specific condition at  $r = r_{in}$ . Thus the accreting mass piles up in the central region.

## 2.5. Initial Perturbation

To initiate the evolution, we imposed random perturbation for the azimuthal velocity with maximum amplitude  $0.01v_0$ . We checked the stability of the initial state by carrying out numerical simulations without including magnetic fields and without imposing velocity perturbations. Since the boundary between the rotating disk and the static corona is not exactly in hydrostatic equilibrium, small motions with maximum velocity  $0.05v_0$  appears in this region. The radial velocity in the dense region of the torus is less than  $0.001v_0$ . The radial flow in the boundary layer between the disk and the corona slightly modifies the density distribution and smears the difference of the rotation speed between the disk and the corona. However, the flow does not significantly modify the density distribution of the main part of the torus. At  $t = 2$  Gyr, the maximum radial speed is about  $0.0045v_0$  even at the interface between the disk and the corona. The torus stays in the equilibrium state for time scale longer than 2.3 Gyrs.

## 3. NUMERICAL RESULTS

### 3.1. Time Evolution of the Model with Absorbing Inner Boundary Condition

First we present the results of Model I (the standard model). The inner boundary is treated as an absorbing boundary where accreting mass and magnetic fields are absorbed. Figure 3 shows the time evolution of model I. Color contours show density distribution and solid curves show magnetic field lines. The left panels show the isosurface of the density ( $\rho/\rho_b = 10^{-1.5}$ ), density distribution at the equatorial plane and magnetic field lines. We plotted the region  $-15 \text{ kpc} < x, y, z < 15 \text{ kpc}$ . The right panels show the equatorial density and magnetic field lines projected onto the equatorial plane. As the MRI grows, matter accretes to the central region by losing the angular momentum. The initial torus deforms itself into a flat disk. On the other hand, the matter in the outer part of the disk gets angular momentum and expands. The magnetic fields globally show spiral structure and locally show turbulent structure.

Figure 4 shows the close up view of the density distribution and magnetic field lines projected onto the equatorial plane at  $t = 1000t_0 (= 3.8 \text{ Gyr})$ . The box size is  $-15 \text{ kpc} <$

$x, y < 15$  kpc. The density distribution shows weak non-axisymmetric spiral pattern.

Figure 5a shows the time evolution of magnetic energy for model I averaged in  $2 \text{ kpc} < \varpi < 5 \text{ kpc}$ ,  $0 \text{ kpc} < z < 1 \text{ kpc}$  and  $0 \leq \varphi < 2\pi$ . Figure 5b shows the plasma  $\beta$  averaged in the same region. As the MRI grows in the disk, the magnetic energy increases and its strength saturates when  $\log[(B^2/8\pi)/P_b] \sim -1.5$ . For our Galaxy, this saturation level corresponds to  $B \sim 3\mu \text{ G}$ . The magnetic energy is maintained for time scale at least 2 Gyrs. As magnetic energy is amplified, the average value of plasma  $\beta \equiv \langle P \rangle / \langle B^2/8\pi \rangle$  decreases and stays around  $\langle \beta \rangle \sim 20$  where  $\langle \beta \rangle$  is the spatial average of local plasma  $\beta$  in  $2.0 \text{ kpc} < \varpi < 5.0 \text{ kpc}$ ,  $0 \text{ kpc} < z < 1.0 \text{ kpc}$  and  $0 \leq \varphi < 2\pi$ . This saturation level of magnetic energy is smaller than that observed in our galaxy. Further amplification of magnetic energy by, for example, supernova explosions may be necessary to explain the strength of magnetic fields in our galaxy.

Magnetic field lines shown in the left panels of figure 3 indicate that magnetic fields initially confined in the disk emerge from the disk and form extended magnetized corona. Figure 6 shows the vertical distribution of the gas pressure and the magnetic pressure at  $\varpi = 3 \text{ kpc}$ ,  $5 \text{ kpc}$  and  $10 \text{ kpc}$  at  $t = 0$  and  $t = 1000t_0 (= 3.8 \text{ Gyr})$ . The magnetic flux initially confined in the torus fills almost the whole simulation region. The plasma  $\beta$  in the corona is  $1 < \beta < 10$  in  $1 \text{ kpc} < z < 10 \text{ kpc}$ .

Magnetic fields emerge from the disk to the corona due to the growth of the Parker instability (Parker 1966). Nonlinear growth of Parker instability in disks was studied by Matsumoto et al. (1988) by two-dimensional MHD simulations taking into account the vertical variation of the gravitational field. The effects of the differential rotation and MRI on the Parker instability were studied by Foglizzo & Tagger (1994, 1995). Miller & Stone (2000) carried out local three-dimensional MHD simulations of gravitationally stratified differentially rotating disks and showed that strongly magnetized corona is created due to the buoyant rise of magnetic flux from the disk to the corona. Machida et al. (2000) showed by global three-dimensional MHD simulations that buoyantly rising magnetic loops are formed above accretion disks. Our numerical results are consistent with these previous results.

Figure 7 shows the radial distribution of azimuthal velocity  $v_\varphi$  and the density  $\rho$  averaged in  $0 \text{ kpc} < z < 0.3 \text{ kpc}$  and  $0 \leq \varphi < 2\pi$  at  $t = 3.8 \text{ Gyr}$ . In the inner region ( $\varpi < 10 \text{ kpc}$ ), the radial profile of azimuthal velocity of model I is similar to that observed in our Galaxy. The density distribution in Figure 7b indicates that the initial torus spreads and becomes flat in the inner region.

Figure 8a shows the time evolution of the ratio of Maxwell stress averaged in  $2 \text{ kpc} <$

$\varpi < 5$  kpc,  $0$  kpc  $< z < 1$  kpc and  $0 \leq \varphi < 2\pi$  to the initial gas pressure at  $\varpi = 10$  kpc,

$$\alpha_B \equiv \left\langle -\frac{B_\varpi B_\varphi}{4\pi P_b} \right\rangle. \quad (15)$$

The Maxwell stress increases as the gas accretes and later decreases gradually.

Figure 8b shows the time evolution of the accretion rate at  $\varpi = 2.5$  kpc defined by

$$\dot{M}_{\varpi=2.5} = - \int_0^{2\pi} \int_0^{2.5\text{kpc}} \rho v_\varpi \varpi d\varphi dz. \quad (16)$$

The unit of the accretion rate is  $1M_\odot/\text{yr}$  when  $\rho_b = 3 \times 10^{-25} \text{ g/cm}^3$ . Numerical result indicates that  $\dot{M} \sim 10^{-3} M_\odot/\text{yr}$ . Since the mass of the initial torus is  $M_{\text{torus}} = 5 \times 10^8 M_\odot$ , mass accretion takes place for time scale longer than 10 Gyr.

### 3.2. Effects of the Central Absorber and Dark Matter

In this subsection, we show the effects of the central absorber and the dark matter. In model I, we assumed that the interstellar matter accreting to the central region are absorbed at  $r = 0.8$  kpc. This mimics the existence of the central black hole or the efficient conversion of gas to stars in the central region. When such absorber does not exist, accreting matter piles up in the central region. As a reference model, we carried out a simulation of model II, in which we allow the accreting mass to pile up in the central region.

Figure 9 shows the density distribution and magnetic field lines at  $t = 1000t_0$  ( $= 3.8$  Gyr) for model II. Since accreted matter accumulates in the central region, it forms a high density bulge.

Figure 10 shows the distribution of density and magnetic field lines at  $t = 3.8$  Gyr for model III. In this model, the effect of dark matter is included. Absorbing boundary condition is imposed at  $r = 0.8$  kpc. The density distribution and magnetic field lines are similar to those of model I.

Figures 11a and 11b show the time evolution of magnetic energy and plasma  $\beta$  averaged in  $2 \text{ kpc} < \varpi < 5 \text{ kpc}$ ,  $0 \text{ kpc} < z < 1 \text{ kpc}$  and  $0 \leq \varphi < 2\pi$ , for models I, II and III. The magnetic energy saturates at approximately the same level for all models. The magnetic energy is maintained more than 2Gyrs. However, after significant amount of gas accretes, the value of plasma  $\beta$  in model II becomes larger than that of other models, because in model II, the gas density and pressure increase with time. Figure 11c shows the ratio of Maxwell stress to gas pressure averaged in  $2 \text{ kpc} < \varpi < 5 \text{ kpc}$ ,  $0 \text{ kpc} < z < 1 \text{ kpc}$  and  $0 \leq \varphi < 2\pi$

for model I, II and III. The time evolution of Maxwell stress has almost the same profile in all models. Figure 11d shows the time evolution of the accretion rate at  $\varpi = 2.5$  kpc for these models. In model II, the accretion rate is about 10 times larger than that of model I and model III because the density near  $\varpi = 2.5$  kpc of model II is larger than the density of model I and model III (see figure 12b).

Figure 12 shows the distribution of azimuthal velocity  $v_\varphi$  and density  $\rho$  averaged in  $0 \text{ kpc} < z < 0.3 \text{ kpc}$  and  $0 \leq \varphi < 2\pi$  at  $t = 3.8 \text{ Gyr}$ . The azimuthal velocity of model I and model III is similar to the observed profile of our Galaxy in the inner region. The velocity profile of model III coincides with the observed profile in all region because the effects of dark matter are included. On the other hand, the velocity distribution of model II is different from the observed rotation curve. In the inner region, the density of model II is ten times larger than that of model I and model III because the accreted gas piles up in the central region. When mass piles up in the central region, since the pressure gradient force in the radial direction reduces the effective gravity in the radial direction, the equilibrium rotation speed becomes much less than the observed rotation speed. Thus, the existence of the central absorber or conversion of infalling gas to stars are essential to reproduce the observed rotation curve. In the outer region ( $8 \text{ kpc} < \varpi$ ) velocity and density of model I and model II almost coincide.

### 3.3. Spatial and Temporal Reversals of Mean Magnetic Fields

Figure 13 shows the magnetic field lines depicted by mean magnetic fields for model III at  $t = 3.8 \text{ Gyr}$ . Regions colored in orange or blue show domains where mean azimuthal magnetic field at  $z = 0.25 \text{ kpc}$  is positive or negative, respectively. The box size is  $30 \text{ kpc} \times 30 \text{ kpc}$ . We computed the mean magnetic field at each grid point

$$\bar{\mathbf{B}}(\varpi_i, \varphi_j, z_k) = \frac{\sum_{l=i-10}^{i+10} \sum_{m=j-3}^{j+3} \sum_{n=k-10}^{k+10} \mathbf{B}(\varpi_l, \varphi_m, z_n)}{21 \times 7 \times 21}, \quad (17)$$

by averaging magnetic fields inside  $\pm 10$  meshes in  $\varpi$  and  $z$  directions, and  $\pm 3$  meshes in  $\varphi$  direction. The mean magnetic field is mainly toroidal but shows reversals of toroidal components around  $\varpi \sim 5 \text{ kpc}$  at this time.

The azimuthal direction of mean magnetic fields in the disk changes with radius in regions where channel-like flow develops. Hawley & Balbus (1992) showed by axisymmetric simulations that channel-like flows appear in the nonlinear stage of MRI. Even when the unperturbed magnetic field is purely azimuthal, spiral channel flows appear as a result of the nonlinear growth of the non-axisymmetric MRI ( Machida & Matsumoto 2003). Since

such magnetic channels move inward as the infalling gas loses angular momentum, the radius of the field reversal changes with time.

Figure 14 shows the azimuthally averaged mean toroidal field  $\langle \bar{B}_\varphi \rangle$  (mean field) and the standard deviation of azimuthal field  $\sqrt{\langle (B_\varphi - \bar{B}_\varphi)^2 \rangle}$  (fluctuating field) at  $t = 3.1$  Gyr where  $\langle \rangle$  denotes the spatial average. The dashed, dotted and solid curves show the distribution of mean azimuthal magnetic fields averaged in azimuthal direction ( $0 \leq \varphi < 2\pi$ ) and in  $0.1 \text{ kpc} < z < 1.0 \text{ kpc}$  (equatorial region),  $1.0 \text{ kpc} < z < 3.0 \text{ kpc}$  (coronal region) and  $0.1 \text{ kpc} < z < 3.0 \text{ kpc}$ , respectively. The vertical bars show the standard deviation of the azimuthal field. The strength of fluctuating field is comparable to the mean magnetic field. The dash-dotted curve shows the initial distribution of azimuthal mean magnetic fields averaged in  $0.3 \text{ kpc} < z < 2.0 \text{ kpc}$  and  $0 \leq \varphi < 2\pi$ . The strength of equatorial azimuthal magnetic field ( $0.1 \text{ kpc} < z < 1 \text{ kpc}$ ) is larger than the initial azimuthal field by factor 2.

The mean azimuthal magnetic field in the coronal region ( $1.0 \text{ kpc} < z < 3.0 \text{ kpc}$ ) has direction opposite to that in the disk region. The total magnetic flux threading the  $\varpi$ - $z$  plane is almost conserved.

Figure 15 shows the spatial distribution of mean azimuthal magnetic fields for model III at  $t = 590t_0 (= 2.2 \text{ Gyr})$  and  $826t_0 (= 3.1 \text{ Gyr})$ . Blue and orange indicate regions where mean magnetic field  $\bar{B}_y$  threading the  $y = 0$  plane is positive or negative, respectively. Arrows show the direction of magnetic fields. These panels show that the mean azimuthal field  $\bar{B}_y$  threading the  $y = 0$  plane reverses its direction in the coronal region. The maximum height of the magnetized region (the wavefront of the azimuthal magnetic field) at  $\varpi = 10 \text{ kpc}$  locates at  $z = 4 \text{ kpc}$  at  $t = 2.2 \text{ Gyr}$  and  $z \sim 10 \text{ kpc}$  at  $t = 3.1 \text{ Gyr}$ . It indicates that the azimuthal magnetic flux is rising.

The seeds for the reversals of the azimuthal magnetic fields are generated during the growth of MRI because when the initial magnetic field is purely azimuthal, the growth rate of the MRI is larger when  $q = (k_y/k_z)^2$  is small, where  $k_y$  and  $k_z$  are the wavenumber in the azimuthal direction and the vertical direction, respectively (e.g., Matsumoto & Tajima 1995). Thus, the azimuthal direction of the perturbed magnetic field changes with height. In the nonlinear stage when the vertical magnetic fields are produced by the buoyant rise of the azimuthal magnetic flux, the formation of the channel flows (e.g., Hawley & Balbus 1992) due to the nonlinear growth of MRI also produces the reversals of azimuthal magnetic fields.

Figure 16a shows the time variation of the vertical distribution of azimuthally averaged magnetic field  $\langle B_\varphi \rangle$  for model III at  $\varpi = 10 \text{ kpc}$ . The regions where  $\langle B_\varphi \rangle < 0$  are not plotted. The wavefront of the azimuthal flux propagates in the vertical direction with speed

$v \sim 8 \text{ kpc}/1.5 \text{ Gyr} \sim 5 \text{ km/s}$ . This speed is comparable to the Alfvén speed. The vertical distribution of the azimuthal field  $\langle B_\varphi \rangle$  approximately follows the self-similar solution of the nonlinear Parker instability  $\langle B_\varphi \rangle \propto z^{-1}$  (Shibata et al. 1989). Figure 16b shows the time evolution of the height of the wavefront of the azimuthal magnetic flux (solid curve) and the height of reversals of azimuthal magnetic fields (dashed curve and dash-dotted curve) at  $\varpi = 10 \text{ kpc}$ . The exponential increase of the height of the wavefront is consistent with the self-similar solutions of the nonlinear Parker instability (Shibata et al. 1989). After an azimuthal magnetic flux with one direction rises, another azimuthal magnetic flux with opposite direction rises. The MRI unstable disk continuously feeds the corona with magnetic fields.

In figure 17 we plotted the time variation of mean azimuthal field of model III. Magnetic fields are averaged in azimuthal direction ( $0 \leq \varphi < 2\pi$ ), radial direction ( $5 \text{ kpc} \leq \varpi < 6 \text{ kpc}$ ), and in  $0.1 \text{ kpc} < z < 1.0 \text{ kpc}$  (equatorial region),  $1.0 \text{ kpc} < z < 3.0 \text{ kpc}$  (coronal region) and  $0.1 \text{ kpc} < z < 3.0 \text{ kpc}$  (disk + corona), respectively. The equatorial magnetic field in  $5 \text{ kpc} < \varpi < 6 \text{ kpc}$  changes direction with time. The azimuthal magnetic fields reverse their direction with timescale  $t \sim 300t_0 (\sim 1 \text{ Gyr})$ . This timescale is comparable to that of the buoyant rise of azimuthal magnetic flux, which takes place in  $t \sim 10H/v_A$ , (e.g., Parker 1966), where  $H$  is the half thickness of the disk ( $\sim 0.5 \text{ kpc}$ ), and  $v_A$  is the Alfvén speed around the disk-corona interface ( $v_A \sim 5 \text{ km/s}$ ).

Here we would like to point out that the amplification of equatorial magnetic field is enabled by the escape of magnetic flux from the disk to the corona. When the total azimuthal magnetic flux is conserved, the azimuthal magnetic flux inside the disk can increase when magnetic flux escapes from the disk to the corona. Although azimuthal magnetic flux is not exactly conserved in resistive MHD simulations, the flux is nearly conserved because  $\eta$  is small. Thus the buoyant escape of azimuthal magnetic flux from the disk to the corona is compensated by the amplification of azimuthal magnetic flux inside the disk with polarity opposite to that in the corona.

### 3.4. Dependence on the Strength of Initial Magnetic Fields

We also carried out a simulation (model IV) starting from the initially weaker magnetic field ( $\beta_b = 1000$ ). In this model, the magnetic energy saturates at almost the same level as in model III ( $B_\varphi \sim 1\mu \text{ G}$  at  $\varpi \sim 5 \text{ kpc}$ ). Figure 18 shows the spatial distribution of mean azimuthal magnetic fields for model IV at  $t = 824t_0 (= 3.1 \text{ Gyr})$  and at  $t = 1115t_0 (= 4.2 \text{ Gyr})$ . Blue and orange indicate regions where mean magnetic field  $\bar{B}_\varphi$  threading the  $y = 0$  plane is positive or negative, respectively. Again, the azimuthal magnetic field changes

direction with radius and with height. The striped distribution of azimuthal magnetic fields and the vertical propagation of the reversals of azimuthal magnetic fields are similar to those in model III (figure 15).

In Figure 19 we plotted the time variation of mean azimuthal field of model IV. Magnetic fields are averaged in azimuthal direction ( $0 \leq \varphi < 2\pi$ ), radial direction ( $5 \text{ kpc} \leq \varpi < 6 \text{ kpc}$ ), and in  $0.1 \text{ kpc} < z < 1.0 \text{ kpc}$  (equatorial region),  $1.0 \text{ kpc} < z < 3.0 \text{ kpc}$  (coronal region) and  $0.1 \text{ kpc} < z < 3.0 \text{ kpc}$  (disk + corona), respectively. These results indicate that the direction of mean azimuthal magnetic field reverses several times. The amplitude of oscillation of azimuthal magnetic fields increases with time. The interval of reversal of azimuthal magnetic fields is  $\sim 1 \text{ Gyr}$  (2 Gyr for a full cycle). This timescale coincides with that in model III, in which the initial plasma  $\beta$  is 100. The direction of azimuthal magnetic field in the coronal region is opposite to that of the equatorial region.

### 3.5. Dependence on the Size of the Azimuthal Region and Mesh Size

In order to study the dependence of numerical results on the size of the azimuthal simulation region and mesh sizes in the azimuthal direction, we carried out simulations in which we used 64 (model V), 32 (model VI) and 16 (model VII) grid points in  $0 \leq \varphi < \pi/2$ . Other parameters are the same as those in model III.

Figure 20a shows the early stage ( $t < 600t_0$ ) of the magnetic field amplification in  $2 \text{ kpc} < \varpi < 5 \text{ kpc}$  and figure 20b shows the time variation of magnetic energy in the nonlinear saturation stage. We found that in the early stage ( $t < 600t_0$ ), the growth of the magnetic energy in model VII is similar to that of model III, which has the same azimuthal grid resolution. In the nonlinear saturation stage (figure 20b), however, the magnetic energy in model VII decreases and becomes smaller than that in model III. These results are consistent with the results of local 3D MHD simulations of accretion disks ( Hawley, Gammie & Balbus 1995), in which they showed that the nonlinear saturation level of the magnetic energy increases with the size of the simulation region.

When the azimuthal size of the simulation region is fixed (model V, VI and VII), the saturation level of the magnetic energy ( $t > 600t_0$ ) is larger in the high resolution model (model V) than that in low resolution models (model VI and VII). This result is also consistent with the results of local 3D MHD simulations of the growth of MRI in accretion disks (e.g., Hawley, Gammie & Balbus 1995, 1996).

The time evolution of the magnetic energy before its saturation (figure 20a) depends on how the gas infalls and carries in magnetic fields. The earlier rise of magnetic energy in

the highest resolution model (model V) is due to the faster growth of the MRI in the torus. The growth rate of the MRI is sensitive to the azimuthal grid resolution because the most unstable wavenumber  $k_{\parallel} \sim \Omega/v_A$ , where  $k_{\parallel}$  is the wavenumber parallel to the unperturbed magnetic fields (e.g., Balbus & Hawley 1992) is hardly resolved in low resolution simulations. When  $\beta \sim 100$ , the most unstable wavelength is  $\lambda_{max} \sim 2\pi v_A/\Omega \sim 2\pi H(2/\beta)^{1/2} \sim H$  where  $H$  is the disk half thickness. Thus,  $\lambda_{max} \sim 0.5$  kpc  $\sim (\pi/2) \times 10$  kpc/30. We need at least 120 mesh points in  $0 < \varphi < \pi/2$  when one wavelength is resolved by 4 mesh points. Thus, in all models we adopted in this paper, the fastest growing mode is not numerically resolved. These estimates indicate that the growth rate of MRI is affected by the grid size and that the growth rate in models III, VI and VII at  $\varpi = 10$  kpc are smaller than that in model V. Therefore, the infall of the torus gas is delayed in low-resolution models.

Let us discuss why magnetic energy in low resolution models (model III and VII) is larger than that in high resolution models (model V and VI) in the nonlinear stage before the saturation ( $t < 600t_0$ ). These magnetic fields are carried into  $2$  kpc  $< \varpi < 5$  kpc with the gas infalling along the channels of magnetic fields. Since non-axisymmetric parasitic instabilities (Goodman & Xu 1994) and magnetic reconnection (e.g., Sano & Inutsuka 2001; Machida & Matsumoto 2003) which break up the channel flow can be captured better in high resolution simulations, the growth rate of the magnetic energy becomes smaller in high resolution models than that in low resolution models.

Figure 21a compares the vertical distribution of azimuthal magnetic fields at  $\varpi = 10$  kpc at  $t = 800t_0$  in model III, V, VI and VII. The region where  $B_{\varphi} < 0$  is not plotted. The azimuthal magnetic flux buoyantly rises into the corona and forms extended magnetized region. Numerical results indicate that the magnetic flux rises faster into the corona in the high resolution model (model V) than low resolution models (model VI and VII). High resolution simulations could resolve the most unstable wavelength of the Parker instability,  $\lambda \sim 10H \sim 5$  kpc in our simulation model (e.g., Parker 1966; Matsumoto et al. 1988). Thus, one wavelength of the Parker unstable loop is well resolved in high resolution model with 64 grid points in  $0 \leq \varphi < \pi/2$  at  $\varpi = 10$  kpc (model V) but hardly resolved in the low resolution model (model VII). This may be the reason why toroidal magnetic flux rises faster in model V than in other models (figure 21b).

When the azimuthal resolution is fixed (model III and VII), the magnetic flux rises faster in the model with larger azimuthal simulation region (model III). This dependence on the azimuthal simulation region comes from the horizontal expansion of the rising magnetic loops (e.g., Shibata et al. 1989). When the horizontal simulation region is restricted, since magnetic tension prevents the escape of the magnetic flux, the speed of the buoyantly rising magnetic loops is reduced.

### 3.6. Difference Between the Rotation Curve of Dark Matter and Gas

Figure 22 compares the rotation curve of stars and dark matter computed from the gravitational potential (dashed curve) and the rotation curves for gas (solid curve) obtained from simulations for model III. The rotation curves of our Galaxy interior to the Sun has been obtained by HI gas (e.g., Gunn, Knapp & Tremaine 1979), and CO ( Burton & Gordon 1978) observations. The rotation speed in  $5 - 10$  kpc from the galactic center is  $220 - 260$  km/s and similar to the rotation speed shown in figure 22. The rotation speed of our galaxy distant from the galactic center ( $\varpi > 10$  kpc) is obtained by radio observation of HI gas (e.g., Merrifield 1992). The rotation speed is nearly flat and  $v_\varphi \sim 240$  km/s. The flat rotation curve is similar to the rotation curve in the outer part of external spiral galaxies (e.g., Rubin et al. 1985). Our numerical result reproduces these flat rotation curves when we use the gravitational potential which includes the dark matter.

Since the rotation curve of our galaxy distant from the galactic center is obtained by radio observations of HI gas, the observationally measured rotation curve is that for the gas. The rotation curve of the neutral hydrogen does not necessarily coincide with that of stars and the dark matter. Since they are almost frozen to the magnetic fields, if the magnetic arm rotates with angular speed different from the dark matter, the neutral hydrogen is not a good tracer of mass distribution in our Galaxy. Battaner et al. (1992) suggested that when magnetic pinch force is large enough, they can explain the observed rotation curve of the Galaxy without dark matter. On the other hand, Sánchez-Salcedo & Reyes-Ruiz (2004) reported that the contribution of the magnetic field to the rotation curve is up to 20 km/s and it is not sufficient to banish the effect of dark matter. Our numerical results indicate that even in the presence of dynamically non-negligible magnetic fields, gas component shows a flat rotation curve similar to that observed by neutral hydrogen. Numerical results for model I indicates that if the dark matter does not exist, gas rotation curve decreases with radius. Thus, the flat rotation curve obtained by observations of neutral hydrogen really indicates the existence of dark matter.

## 4. Summary and Discussion

We carried out global three-dimensional magnetohydrodynamic (MHD) simulations of galactic gaseous disks to investigate how the galactic magnetic fields are amplified and maintained. We showed the dependence of numerical results on physical conditions in the innermost region, gravitational potential, and strength of initial magnetic fields.

In all models, the magnetorotational instability (MRI) grows in the disk and the mag-

netic energy is amplified and maintained for more than 5 Gyrs. The saturation level of magnetic fields, however, is smaller than that expected from observations ( $B \sim$  several  $\mu G$ ) at  $\varpi = 10$  kpc. The multiphase nature of interstellar space, supernova explosions, cosmic rays and/or non-axisymmetric spiral potential may be important to further amplify magnetic fields.

Numerical results indicate that mean azimuthal field inside the galactic disk is amplified and that its direction changes quasi-periodically. The amplitude of the oscillation of the azimuthal field increases with time. The interval of reversal of equatorial azimuthal field is  $\sim 1$  Gyr. This timescale is comparable to the timescale of the buoyant rise of azimuthal magnetic flux from the disk to the corona. The amplitude of the fluctuating field is comparable to the mean magnetic field. The strength of the mean field only weakly depends on the initial strength of magnetic fields. In the coronal region, the mean azimuthal field has direction opposite to the mean field of the disk.

Mean magnetic fields obtained from numerical simulations also show reversals in the radial direction near the equatorial plane around  $\varpi = 5$  kpc at  $t = 3.8$  Gyr. The radius of the field reversal changes with time because the spiral magnetic channels which produce the reversal of azimuthal fields in the radial direction move inward as the disk gas accretes toward the galactic center.

In the Galactic plane, magnetic field reversals are observed by Rotation Measure (RMs) of pulsars (e.g., Han et al. 2002). The reversals of mean magnetic fields are observed in our Galaxy between the local Orion arm and the inner Sagittarius arm ( Simard-Normandin & Kronberg 1979). More recent analysis imply axisymmetric field with two reversals ( Rand & Kulkarni 1989; Rand & Lyne 1994; see also Beck et al. 1996). Simulation results of model III (Figure 13) show reversals of mean magnetic fields near the equatorial plane around  $\varpi = 5$  kpc. Note that RMs measure the mean magnetic field in some specific direction from the Earth. When we draw lines from a point in Figure 13, we can see field reversals in several directions. Since the magnetic fields inside the galactic disk is turbulent, more and more field reversals will be observed as angular resolution of RMs increase.

In conventional theories of  $\alpha\omega$ -dynamos, various kinds of spatial and temporal oscillations appear depending on the dynamo number  $D = C_\alpha C_\Omega$  where  $C_\Omega = H^2\Omega/\eta$  ( $H$  is the thickness of the disk,  $\Omega$  is the rotation angular speed and  $\eta$  is the magnetic diffusivity) and  $C_\alpha = H\alpha/\eta$  (e.g., Stepinski & Levy 1988). In our global MHD simulations, we do not need to introduce the dynamo  $\alpha$  parameter. The amplification of magnetic fields due to MRI and the reproduction of toroidal fields through gas motions are self-consistently incorporated in our simulations. We introduced anomalous resistivity  $\eta$  to handle magnetic reconnection which takes place in local region where current sheets are formed, but the turbulent diffu-

sivity is not explicitly assumed. We showed by direct 3D simulations that mean toroidal magnetic fields show reversals both in space and time.

Tout & Pringle (1992) constructed phenomenological models of disk dynamos by taking into account the growth of magnetic fields due to MRI, escape of magnetic flux by the Parker instability, and the dissipation of magnetic fields by magnetic reconnection. They showed that the magnetic fields in the disk oscillate quasi-periodically with period comparable to the time scale of the buoyant escape of the magnetic flux. This timescale is consistent with the timescale of field reversals obtained from our MHD simulations.

Let us discuss the similarities and dissimilarities of the magnetic activity of galactic gas disks produced by our numerical simulations and those in the Sun. Both objects are differentially rotating plasma with high conductivity in which magnetic fields are almost frozen to the rotating plasma. Thus the magnetic fields can be deformed and amplified by the plasma motion.

The Sun is a slow rotator in which the centrifugal force is much smaller than the gravity, thus its atmosphere is confined by the gravity. The convective motions and/or the differential rotation in the convection region may be the source of magnetic field amplification in the Sun. However, since the magnetic flux tube in the convection region buoyantly rises with a timescale of the order of a month (e. g., Parker 1975), much shorter than the solar magnetic cycle ( $\sim 22$  year), solar dynamo activity is considered to be operating in the interface between the convection zone and the radiative zone, where magnetic buoyancy is small and differential rotation exists (e. g., Spiegel & Weiss 1980; Schmitt & Rosner 1983). On the other hand, galactic gas disks are supported by the rotation and subject to differential rotation, which induces the growth of MRI in the whole disk. In galactic gas disks, since the gas disk is convectively stable, the buoyant escape of the magnetic flux takes place with timescale  $t_{buoy} \sim 10H/v_A \sim 10(1/\Omega)(\beta/2)^{1/2}$ . This timescale is longer than the growth time of MRI  $t_{MRI} \sim 1/\Omega$ . Thus the magnetic fields can be amplified in the disk before escaping to the corona.

Numerical results indicate that the total azimuthal magnetic flux is nearly conserved. When turbulent diffusivity exists, the azimuthal magnetic flux is not necessarily conserved. In our simulations, however, since magnetic diffusion only exists in the local current sheet, the magnetic flux is almost conserved. We found that the toroidal magnetic flux in the disk buoyantly rises into the corona. This result indicates that the buoyant escape of the magnetic flux from the disk enables the amplification of mean magnetic fields in the galactic gas disk. When the magnetic diffusion is not negligible, the total azimuthal magnetic flux is not conserved but the magnetic helicity is conserved. Blackman & Brandenburg (2003) pointed out the importance of helicity conservation and the role of coronal mass ejections,

which help sustaining the solar dynamo cycle. In our simulations, buoyantly rising magnetic loops carry helicity as well as the magnetic flux threading the disk. This escape of magnetic flux and helicity enable the disk to amplify the azimuthal magnetic flux in the equatorial region.

We showed that when we remove the central absorber at  $r = 0.8$  kpc, formation of dense gas bulge forces the rotation curve to deviate from that expected from the gravitational potential (model II). This indicates that in the central region of the galaxy, the gas absorption or the conversion of the accumulated gas to stars are essential to explain the observed rotation curve. The mass accretion rate to the central region is  $\sim 10^{-3} M_{\odot}/\text{yr}$  when we adopt the absorbing boundary condition. This accretion rate depends on the initial density of the torus, which can be formed by the infall of intergalactic matter or by the supernova explosions after bursts of star formation in the certain radius of the disk. When the galaxy was more gas rich in the early stage of its evolution, the accretion rate should be much higher.

We also showed that the gas rotation curve approximately coincides with the rotation curve for stars and dark matter even when magnetic fields are dynamically important. This justifies us to use the gas rotation curve to estimate the distribution of the dark matter.

We thank Drs. T. Kuwabara, S. Miyaji and K. Shibata for discussion. Discussions at IAU XXXth General Assembly, 2003 and the workshop on Magnetic Fields in the Universe, 2004 helped us to complete this work. This work is supported by the Grants-in Aid of Ministry of Education, Science, Sports and Culture (16340052, P.I., R. Matsumoto) the priority research project of the Graduate School of Science and Technology, Chiba University, ACT-JST of the Japan Science and Technology corporation, and UK-Japan collaboration on magnetic activities of the Sun, Stars and accretion disks (P.I., K. Shibata and N. Weiss). Numerical computations were carried out on VPP5000 at the Astronomical Data Analysis Center of the National Astronomical Observatory, Japan (NAOJ).

## REFERENCES

Balbus, S. A., & Hawley, J. F. 1991, ApJ, 376, 214  
Balbus, S. A., & Hawley, J. F. 1992, ApJ, 400, 610  
Battaner, E., Garrido, J. L., Membrado, M., & Florido, E. 1992, Nature, 360, 652  
Beck, R., Brandenburg, A., Moss, D., Shukurov, A., & Sokoloff, D. 1996, ARA&A, 34, 155  
Blackman, E. G., & Brandenburg, A. 2003, ApJ, 584, 99

Brandenburg, A., Krause, F. Meinel, R., Moss, D., & Tuominen, I. 1989, A&A, 213, 411

Brandenburg, A., Donner, K. J., Moss, D., Shukurov, A., Sokolov, D. D., & Tuominen, I. 1992, A&A, 259, 453

Brandenburg, A., Nordlund, A., Stein, R. F., & Torkelsson, U. 1995, ApJ, 446, 741

Burton, W. B., & Gordon, M. A. 1978, A&A, 63, 7

Dziourkevitch, N., & Elstner, D. 2003, Ap&SS, 284, 757

Dziourkevitch, N., Elstner, D., & Rüdiger, G. 2004, A&A, 423, L29

Foglizzo, T., & Tagger, M. 1994, A&A, 287, 297

Foglizzo, T., & Tagger, M. 1995, A&A, 301, 293

Goodman, J., & Xu, G. 1994, ApJ, 432, 213

Gunn, J. E., Knapp, G. R., & Tremaine, S. D. 1979, AJ, 84, 1181

Han, J. L., Manchester, R. N., Lyne, A. G., & Qiao, G. J. 2002, ApJ, 570, L17

Hawley, J. F., & Balbus, S. A. 1992, ApJ, 400, 595

Hawley, J. F., Gammie, C. F., & Balbus, S. A. 1995, ApJ, 440, 742

Hawley, J. F., Gammie, C. F., & Balbus, S. A. 1996, ApJ, 464, 690

Hawley, J. F. 2000, ApJ, 528, 462

Hayashi, M. R., Shibata, K., & Matsumoto, R. 1996, ApJ, 468L, 37

Kato, Y., Mineshige, S., & Shibata, K. 2004, ApJ, 605, 307

Kim, W. T., Ostriker, E. C., & Stone, J. M. 2003, ApJ, 599, 1157

Kitchatinov, L. L., & Rüdiger, G. 2004, A&A, 424, 565

Machida, M., Hayashi, M. R., & Matsumoto, R. 2000, ApJ, 532, L67

Machida, M., & Matsumoto, R. 2003, ApJ, 585, 429

Matsumoto, R., Horiuchi, T., Shibata, K., & Hanawa, T. 1988, PASJ, 40, 171

Matsumoto, R., & Tajima, T. 1995, ApJ, 445, 767

Matsumoto, R., Uchida, Y., Hirose, S., Shibata, K., Hayashi, M. R., Ferrari, A., Bodo, G., & Norman, C. 1996, *ApJ*, 461, 115

Matsumoto, R. 1999, in *Numerical Astrophysics*, ed. Miyama, S. M., Tomisaka, K., & Hanawa, T. (Amsterdam: Kluwer Academic Publishers) 195

Merrifield, M. R. 1992, *AJ*, 103, 1552

Miller, K. A., & Stone, J. M. 2000, *ApJ*, 534, 398

Miyamoto, M., & Nagai, R. 1975, *PASJ*, 27, 533

Miyamoto, M., Satoh, C., & Ohashi, M. 1980, *A&A*, 90, 215

Okada, R., Fukue, J., & Matsumoto, R. 1989, *PASJ*, 41, 133

Parker, E. N. 1966, *ApJ*, 145, 811

Parker, E. N. 1971, *ApJ*, 163, 255

Parker, E. N. 1975, *ApJ*, 198, 205

Piontek, R. A., & Ostriker, E. C. 2004, *ApJ*, 601, 905

Rand, R. J., & Kulkarni, S. R. 1989, *BAAS*, 21, 1188

Rand, R. J., & Lyne, A. G. 1994, *MNRAS*, 268, 497

Richtmyer, R. O., & Morton, K. W. 1967, *Differential Methods for Initial Value Problem* (2d ed., New York: Wiley)

Rubin, E., & Burstein, S., Z. 1967, *J. Comput. Phys.*, 2, 178

Rubin, V. C., Burstein, D., Ford, W. K., & Thonnard, N. 1985, *ApJ*, 289, 81

Sánchez-Salcedo, F. J., & Reyes-Ruiz, M. 2004, *ApJ*, 607, 247

Sano, T., & Inutsuka, S. 2001, *ApJ*, 561, 179

Schmitt, D., & Schüssler M., 1989, *A&A*, 223, 343

Schmitt, J. H. M. M., & Rosner, R. 1983, *ApJ*, 265, 901

Sellwood, J. A., & Balbus, S. A., 1999, *ApJ*, 511, 660

Shibata, K., & Uchida, Y. 1985, *PASJ*, 37, 31

Shibata, K., Tajima, T., Steinolfson, R. S. & Matsumoto, R. 1989, *ApJ*, 345, 584

Simard-Normandin, M., & Kronberg, P. P. 1979, *Nature*, 279, 115

Sofue, Y., Fujimoto, M., & Wielebinski, R. 1986, *ARA&A*, 24, 459

Spiegel, E. A., & Weiss, N. O. 1980, *Nature*, 287, 616

Stepinski, T. F., & Levy, E. H. 1988, *ApJ*, 331, 416

Tout, C. A., & Pringle, J. E. 1992, *MNRAS*, 259, 604

Yokoyama, T., & Shibata, K. 1994, *ApJ*, 436, L197

Table 1. Model parameters and inner boundary conditions

Models	$a_1$	$a_2$	$a_3$	$b_1$	$b_2$	$b_3$	$M_1$	$M_2$	$M_3$	$\beta_b$	Boundary
Model I	0.0	7.258	0.0	0.495	0.520	0.0	2.05	25.47	0.0	100	Absorbing
Model II	0.0	7.258	0.0	0.495	0.520	0.0	2.05	25.47	0.0	100	Non-Absorbing
Model III	0.0	6.2	0.0	0.47	0.15	31.2	1.95	17.4	73.5	100	Absorbing
Model IV	0.0	6.2	0.0	0.47	0.15	31.2	1.95	17.4	73.5	1000	Absorbing
Model V-VII	0.0	6.2	0.0	0.47	0.15	31.2	1.95	17.4	73.5	100	Absorbing

Table 2. Azimuthal grid size, number of grid points in azimuthal direction ( $N_\varphi$ ), and the azimuthal size of the simulation region

Models	$\Delta\varphi$	$N_\varphi$	simulation region
Model I-IV	$\pi/32$	64	$0 \leq \varphi < 2\pi$
Model V	$\pi/128$	64	$0 \leq \varphi < \pi/2$
Model VI	$\pi/64$	32	$0 \leq \varphi < \pi/2$
Model VII	$\pi/32$	16	$0 \leq \varphi < \pi/2$

Note. — Other parameters of model V, VI and VII are the same as those in model III.

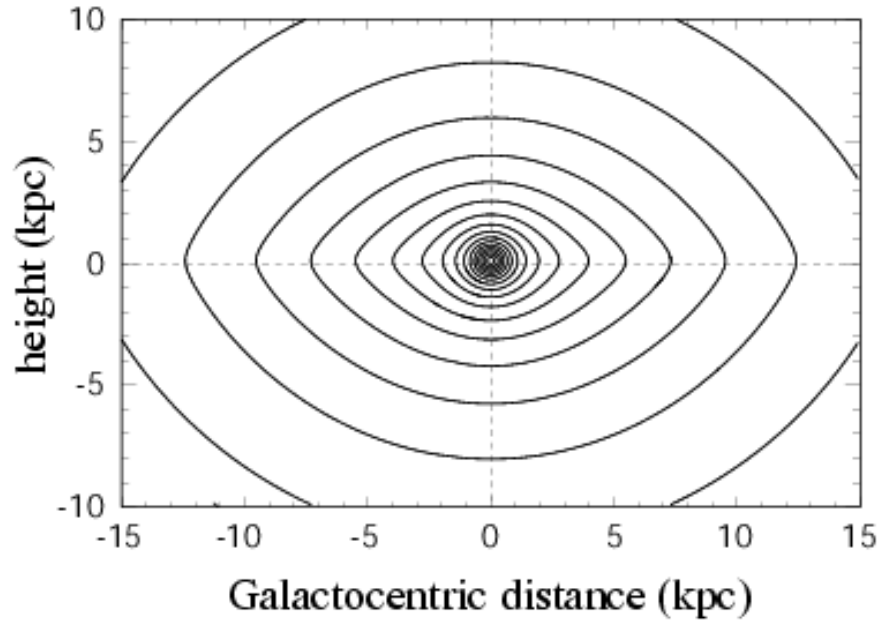


Fig. 1.— Isocontours of the gravitational potential in Miyamoto & Nagai's (1975) model. This potential for model I does not include the effects of dark matter.

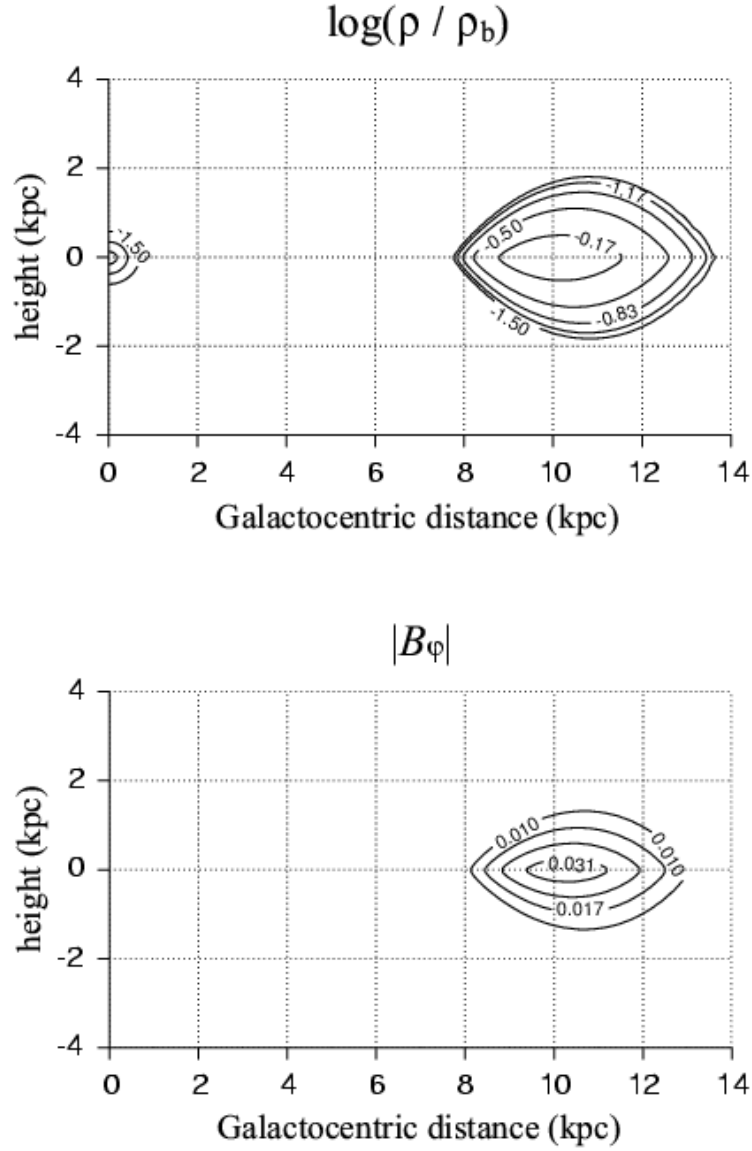


Fig. 2.— Isocontours of initial density distribution (upper panel) and azimuthal magnetic field (bottom panel) for model I.

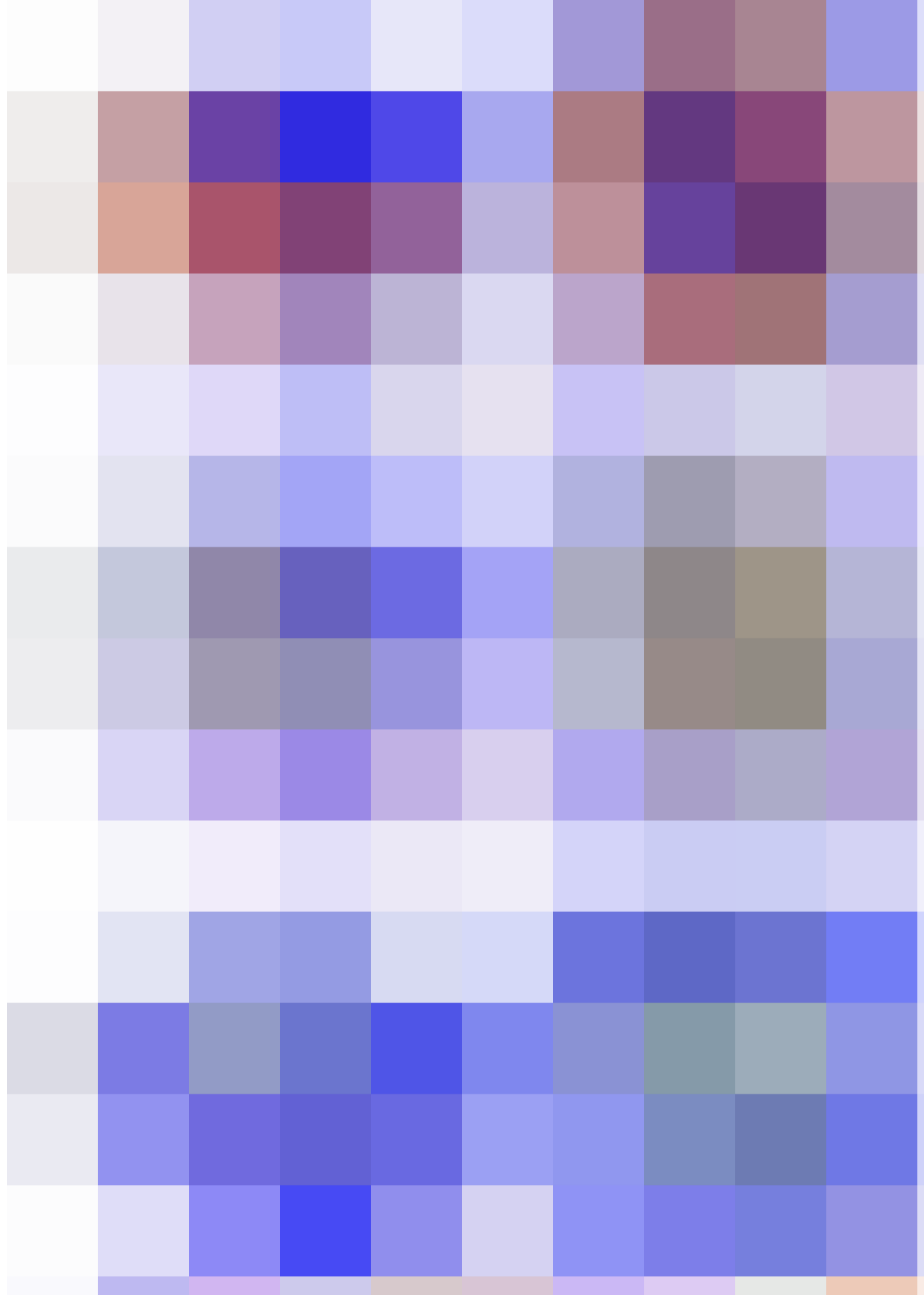


Fig. 3.— Time evolution of density distribution  $\log(\rho/\rho_b)$  (color scale) and magnetic field lines (gray curves) in model I. The box size of left and right panels are  $30 \text{ kpc} \times 30 \text{ kpc} \times 30 \text{ kpc}$  and  $30 \text{ kpc} \times 30 \text{ kpc}$ , respectively. The right panels show the equatorial density and magnetic field lines projected onto the equatorial plane.

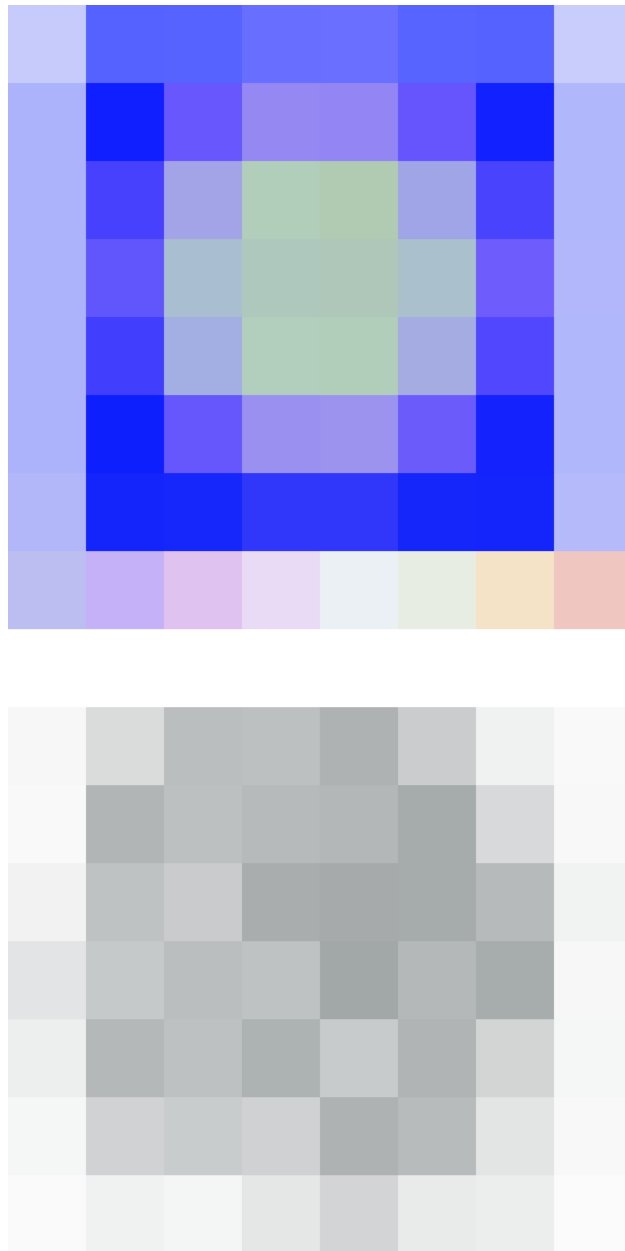


Fig. 4.— Upper panel: The distribution of density  $\log(\rho/\rho_b)$  for model I in the equatorial plane at  $t = 3.8$  Gyr. Lower panel: magnetic field lines in model I projected onto the equatorial plane at  $t = 3.8$  Gyr. The box size is  $30$  kpc  $\times$   $30$  kpc.

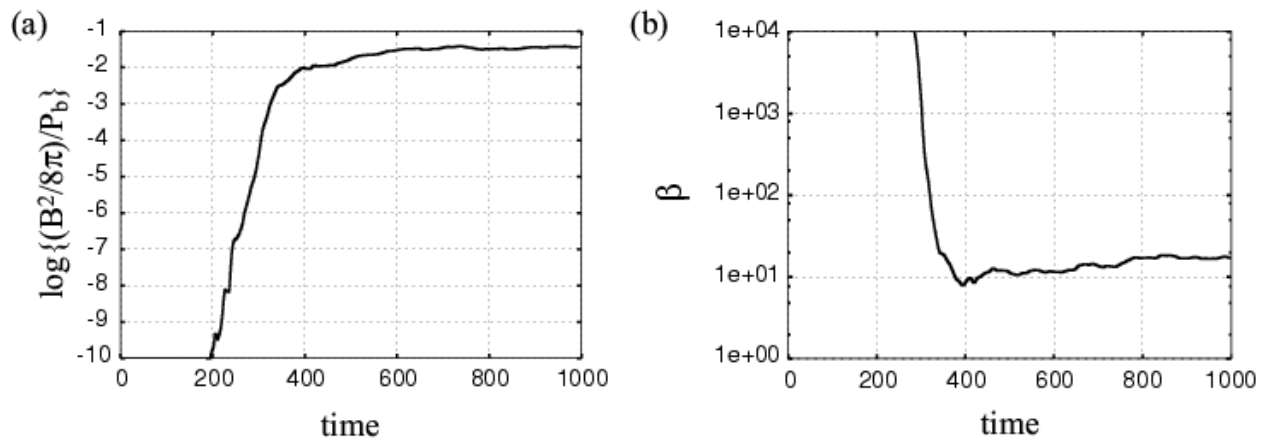


Fig. 5.— (a) Time evolution of the magnetic energy and (b) volume averaged plasma  $\beta$  ( $= \langle P \rangle / \langle B^2 / 8\pi \rangle$ ) for model I averaged in  $2 \text{ kpc} < \varpi < 5 \text{ kpc}$ ,  $0 \text{ kpc} < z < 1 \text{ kpc}$  and  $0 \leq \varphi < 2\pi$ .

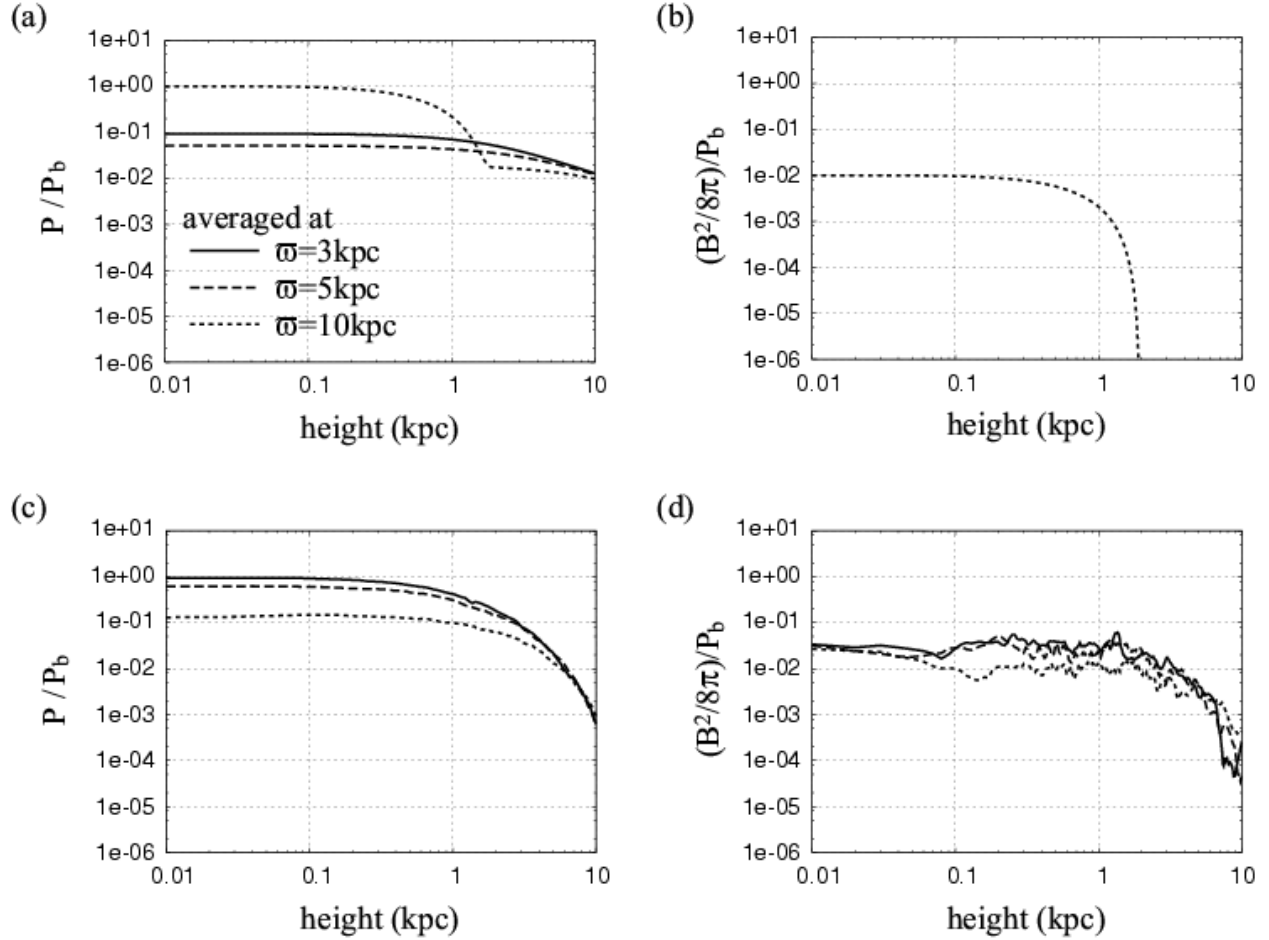


Fig. 6.— Vertical distribution of the gas pressure and magnetic pressure. (a) Initial distribution of gas pressure. (b) Initial distribution of magnetic pressure (c) vertical distribution of gas pressure at  $t = 1000t_0$  and (d) the vertical distribution of magnetic pressure at  $t = 1000t_0$ . The solid, dashed and dotted curves indicate quantities averaged at  $\varpi = 3$  kpc, 5 kpc and 10 kpc, respectively.

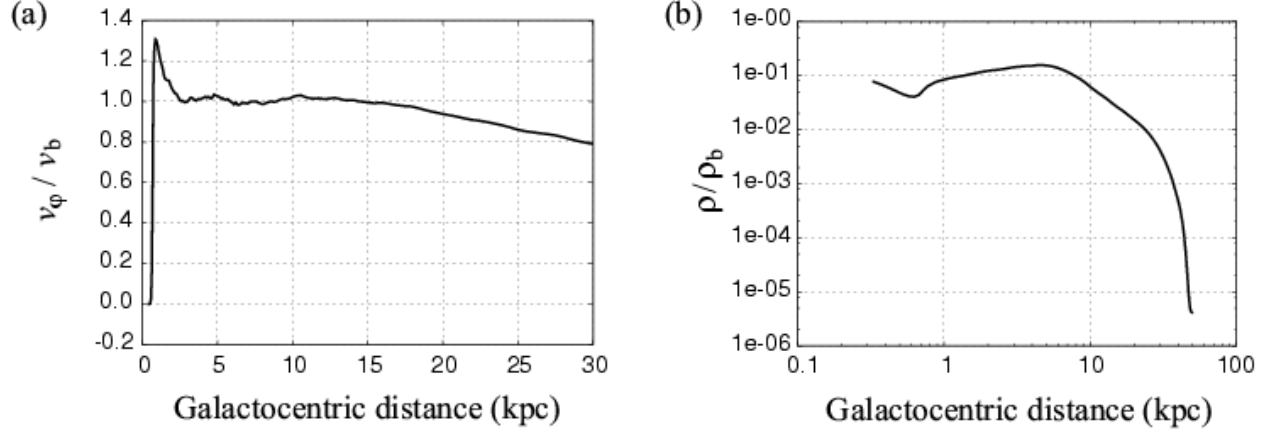


Fig. 7.— The distribution of (a)azimuthal velocity and (b)density  $\rho$  at  $t = 3.8$  Gyr averaged in  $0 \text{ kpc} < z < 0.3 \text{ kpc}$  and  $0 \leq \varphi < 2\pi$  for model I.

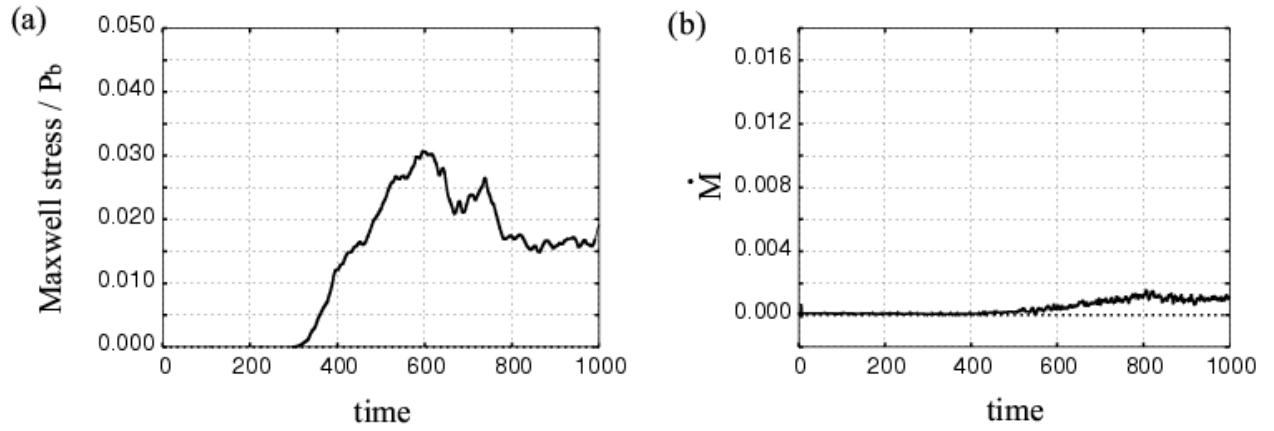


Fig. 8.— (a)Time evolution of Maxwell stress normalized by  $P_b$  for model I. The Maxwell stress is averaged in  $2 \text{ kpc} < \varpi < 5 \text{ kpc}$ ,  $0 \text{ kpc} < z < 1 \text{ kpc}$  and  $0 \leq \varphi < 2\pi$ . (b)Time evolution of the accretion rate at 2.5 kpc from the center. The unit of the accretion rate is  $\dot{M}_0 = 1M_\odot / \text{yr}$  when  $\rho_b = 3 \times 10^{-25} \text{ g/cm}^3$ .

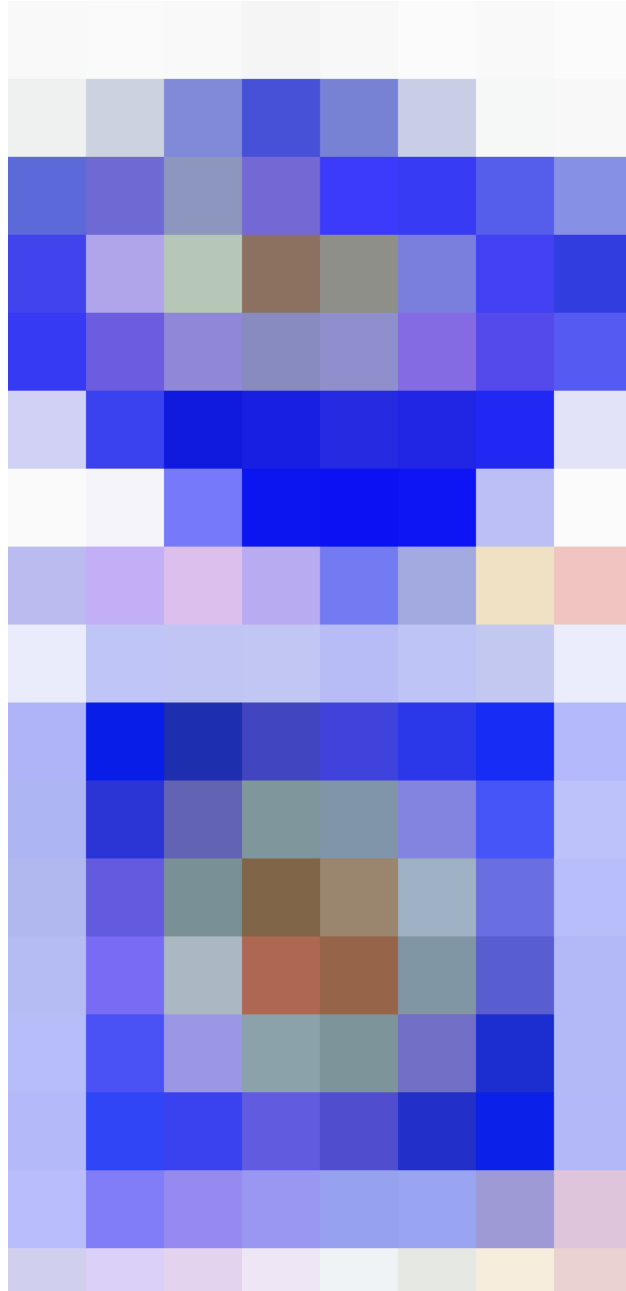


Fig. 9.— The distribution of density (color scale) and magnetic field lines (gray curves) at  $t = 3.8$  Gyr for model II. The box size is  $30 \text{ kpc} \times 30 \text{ kpc}$ .

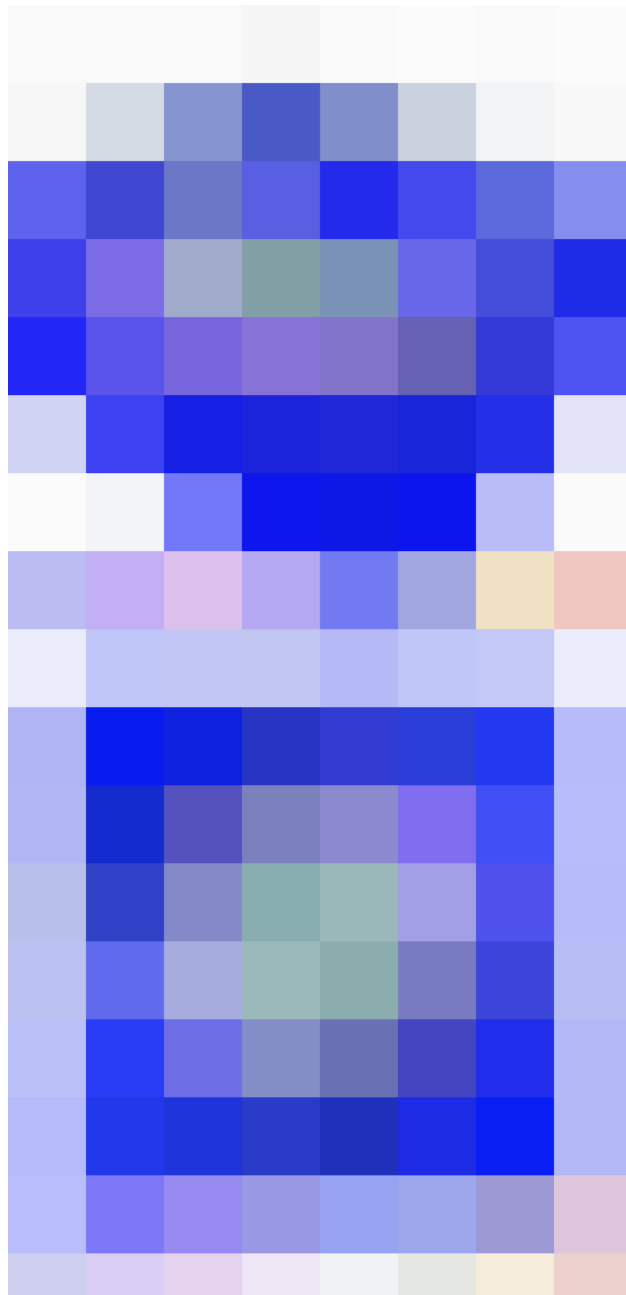


Fig. 10.— The distribution of density (color scale) and magnetic field lines (gray curves) at  $t = 3.8$  Gyr for model III. The box size is  $30$  kpc  $\times$   $30$  kpc.

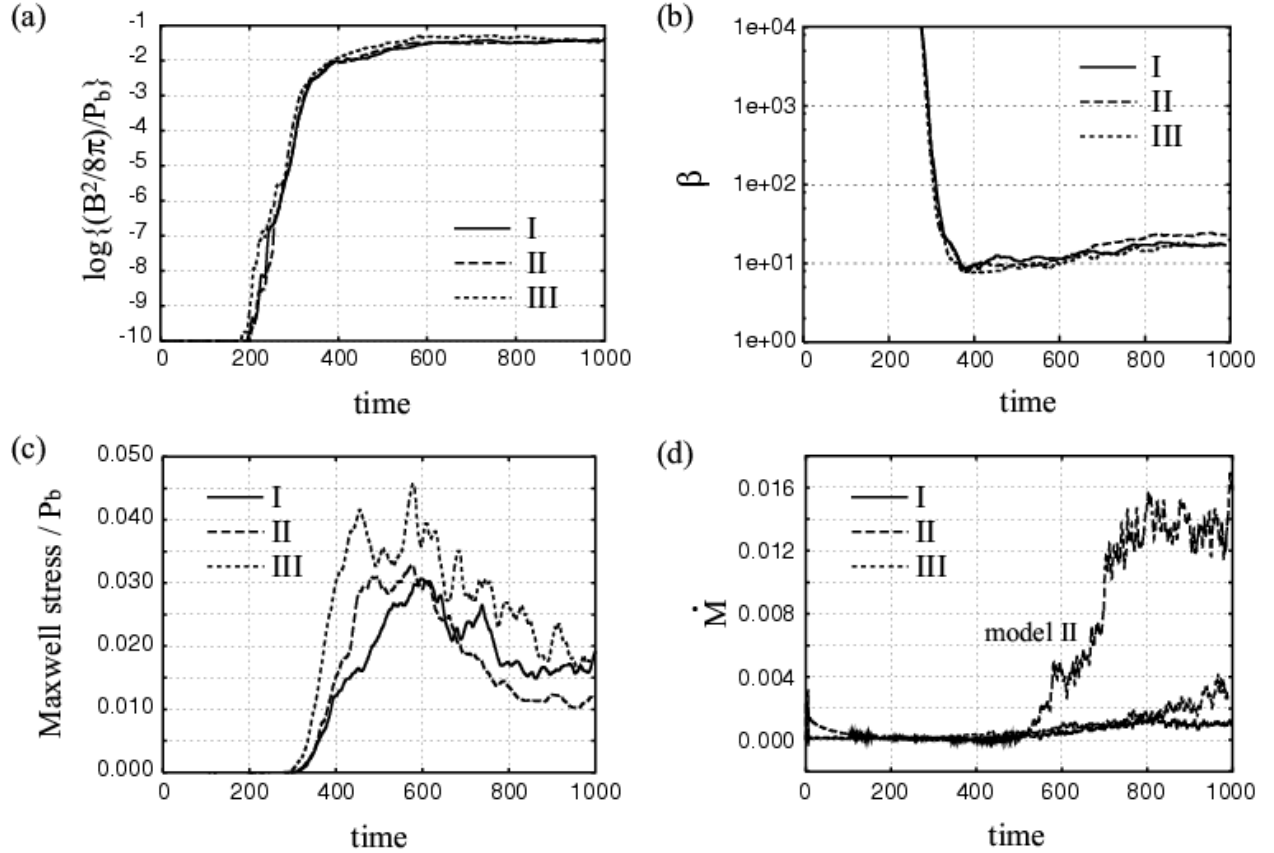


Fig. 11.— Comparison of numerical results for model I, model II and model III. (a) Time evolution of the magnetic energy. (b) Time evolution of the plasma  $\beta$  averaged in  $2 \text{ kpc} < \varpi < 5 \text{ kpc}$ ,  $0 \text{ kpc} < z < 1 \text{ kpc}$  and  $0 \leq \varphi < 2\pi$ . (c) Maxwell stress averaged in the same region. The solid, dashed and dotted curves show the results for model I, model II and model III, respectively. (d) The time evolution of the accretion rate at 2.5 kpc from the center.

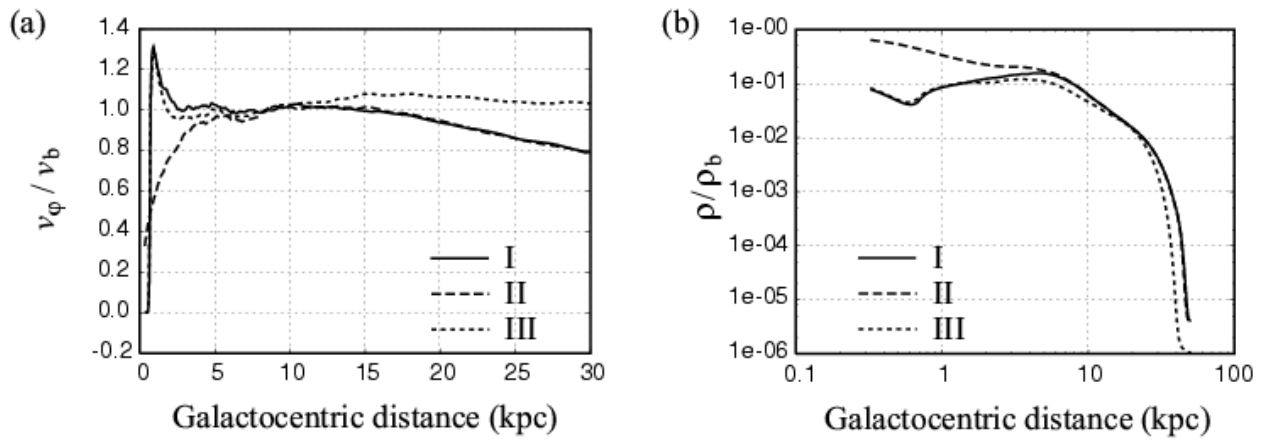


Fig. 12.— (a) The radial distribution of azimuthal velocity  $v_\varphi$  and (b) radial distribution of density  $\rho$  averaged in  $0 \text{ kpc} < z < 0.3 \text{ kpc}$  and  $0 \leq \varphi < 2\pi$  at  $t = 3.8 \text{ Gyr}$ . The solid, dashed and dotted curves show the results for model I, model II and model III, respectively.

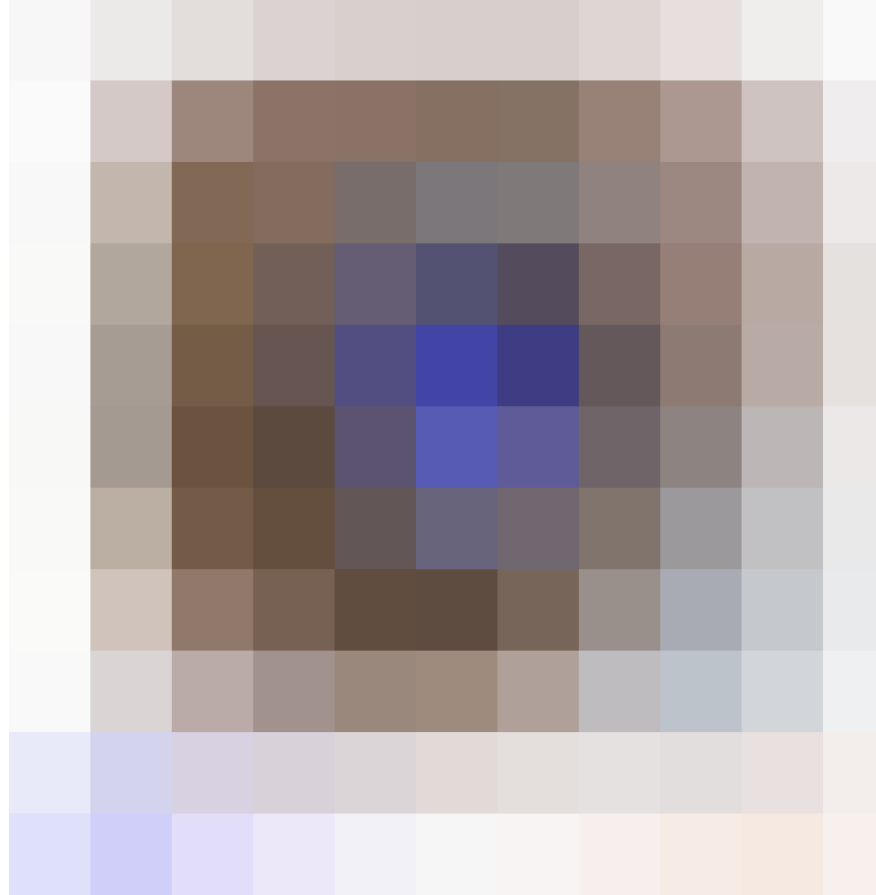


Fig. 13.— Magnetic field lines depicted by mean magnetic fields (solid curves) and isocontours of azimuthal component of magnetic fields at  $z = 0.25$  kpc (color) at  $t = 3.8$  Gyr for model III. Regions colored in orange or blue show domains where azimuthal magnetic field at  $z = 0.25$  kpc is positive or negative, respectively. The box size is  $30$  kpc  $\times$   $30$  kpc.

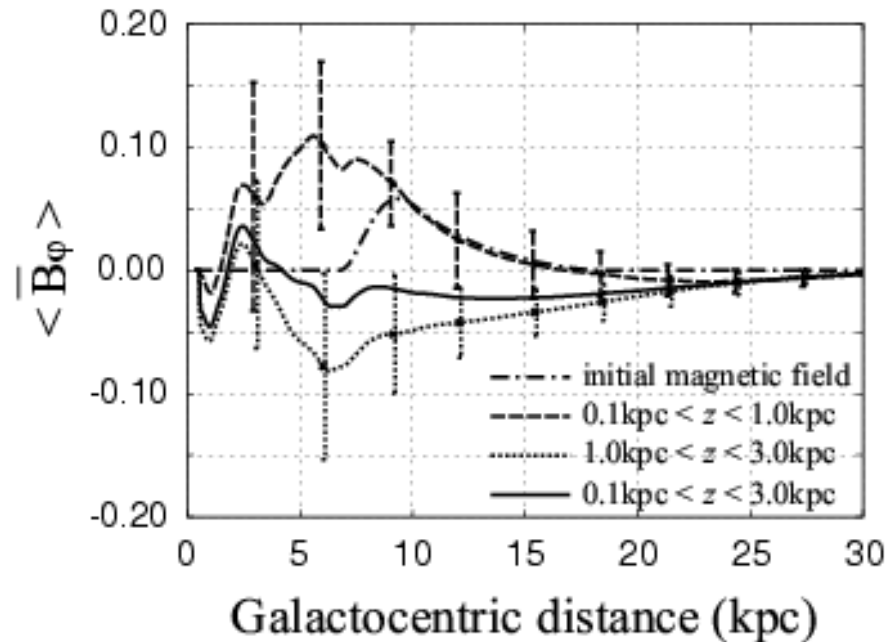


Fig. 14.— Mean azimuthal field and its standard deviation (vertical bars) for model III at  $t = 3.1$  Gyr averaged in azimuthal direction ( $0 \leq \varphi < 2\pi$ ) and in  $0.1 \text{ kpc} < z < 1 \text{ kpc}$  (dashed curve),  $1.0 \text{ kpc} < z < 3.0 \text{ kpc}$  (dotted curve) and  $0.1 \text{ kpc} < z < 3.0 \text{ kpc}$  (solid curve), respectively. The unit of  $B_\varphi$  is  $\sqrt{\rho_b v_0^2} = 15\mu \text{ G}$  in this model when  $\rho_b = 3 \times 10^{-25} \text{ g/cm}^3$ .

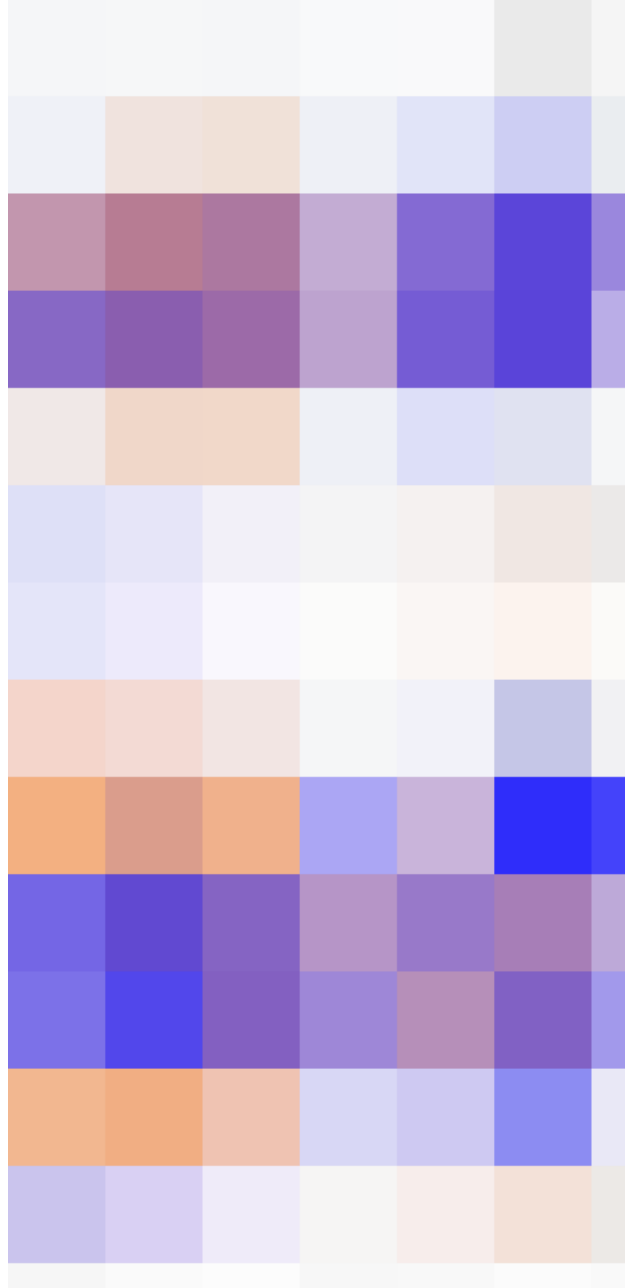


Fig. 15.— The distribution of mean azimuthal magnetic fields for model III at  $t = 590t_0$  ( $= 2.2$  Gyr) and  $826t_0$  ( $= 3.1$  Gyr). Blue and orange indicate regions where the mean field  $\bar{B}_y$  threading the  $y = 0$  plane is positive or negative, respectively. Arrows show the direction of mean magnetic fields. The mean azimuthal fields change their direction with height from the equatorial plane.

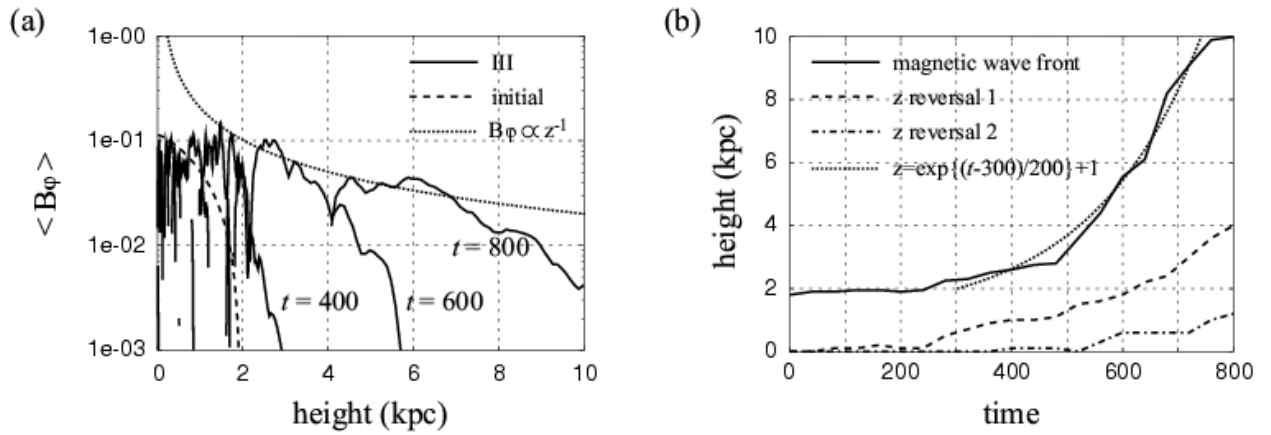


Fig. 16.— (a) Vertical distribution of azimuthally averaged magnetic field  $\langle B_\varphi \rangle$  at  $\varpi = 10$  kpc at  $t = 400t_0$ ,  $600t_0$  and  $800t_0$  for model III. The dashed curve shows the initial profile of  $\langle B_\varphi \rangle$ . The dotted curve shows the  $B_\varphi \propto z^{-1}$  relation expected from the nonlinear theory of the Parker instability. (b) The time evolution of the wave front of rising magnetic flux where  $B_\varphi = 0.003\sqrt{\rho_b v_0^2}$  (solid curve) and the height of where direction of azimuthal magnetic field reverses (dashed curve and dash-dotted curve) for model III. The dotted curve shows the relation  $z = 1 + \exp \{(t - 300)/200\}$  expected from the nonlinear theory of the Parker instability.

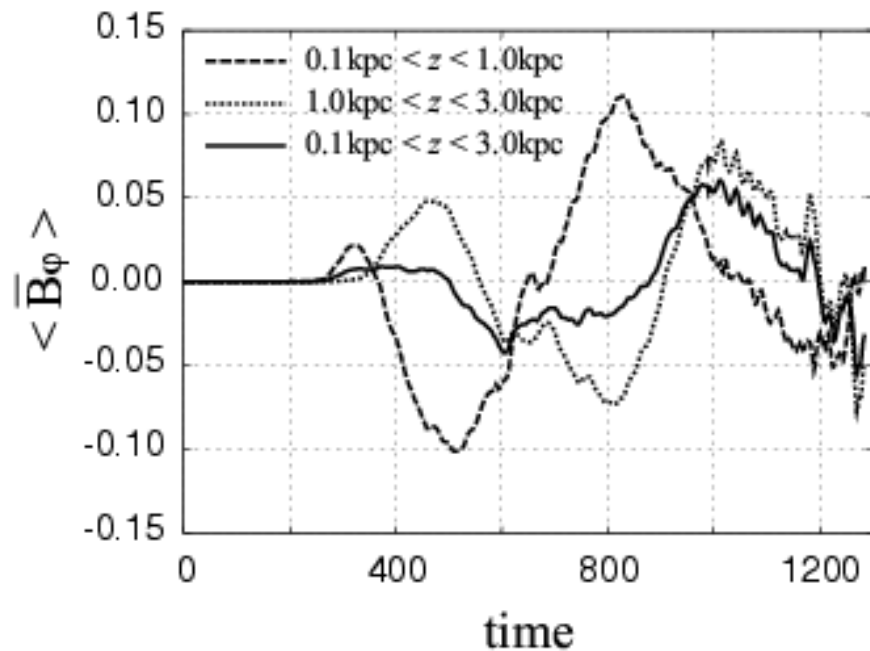


Fig. 17.— The time variation of mean azimuthal field of model III averaged in  $5 \text{ kpc} < \varpi < 6 \text{ kpc}$ ,  $0 \leq \varphi < 2\pi$  and  $0.1 \text{ kpc} < z < 1 \text{ kpc}$  (dashed curve),  $1.0 \text{ kpc} < z < 3.0 \text{ kpc}$  (dotted curve) and  $0.1 \text{ kpc} < z < 3.0 \text{ kpc}$  (solid curve), respectively. The unit of  $B_\varphi$  is  $\sqrt{\rho_b v_0^2} = 15\mu \text{ G}$  in this model when  $\rho_b = 3 \times 10^{-25} \text{ g/cm}^3$ .

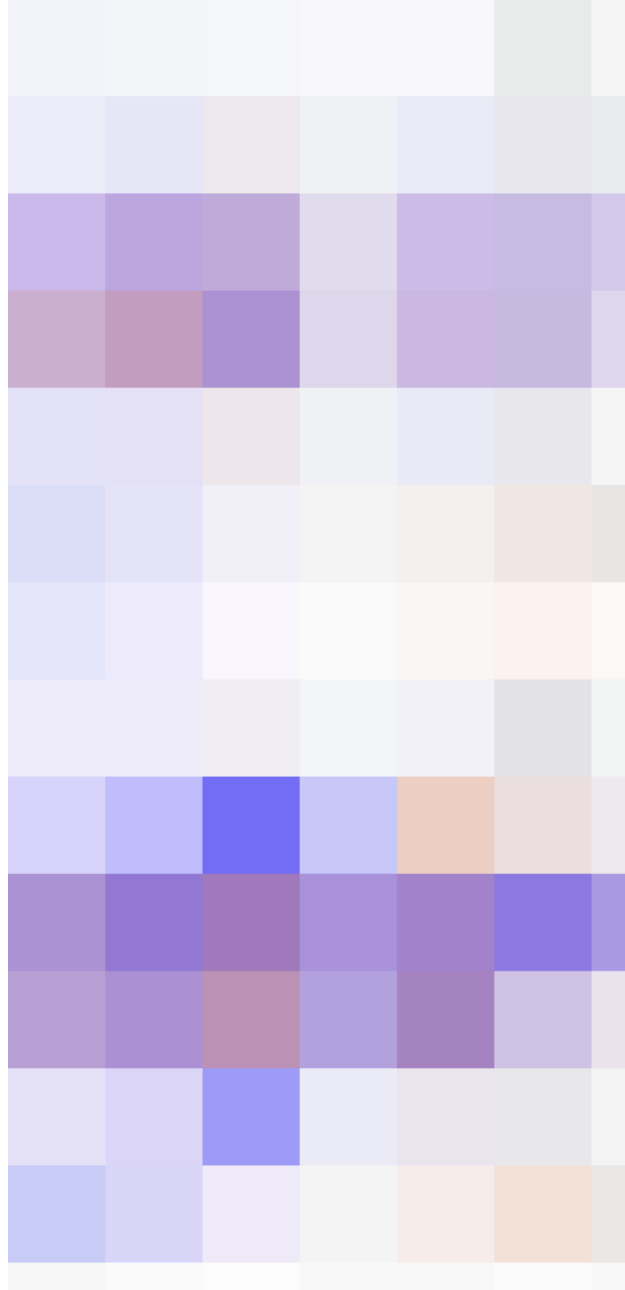


Fig. 18.— The distribution of mean azimuthal magnetic fields for model IV ( $\beta_b = 1000$ ) at (a)  $t = 824t_0$  ( $= 3.1$  Gyr) and (b)  $t = 1115t_0$  ( $= 4.2$  Gyr). Blue and orange indicate regions where the mean field  $\bar{B}_y$  threading the  $y = 0$  plane is positive or negative, respectively. Arrows show the direction of mean magnetic fields. The mean azimuthal fields change their direction with height from the equatorial plane.

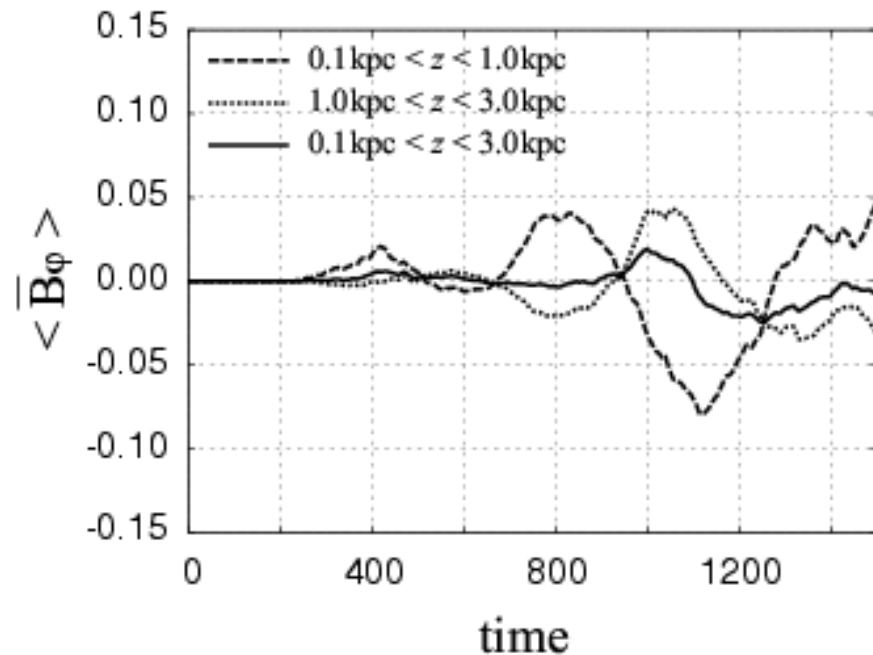


Fig. 19.— The time variation of mean azimuthal field of model IV averaged in  $5 \text{ kpc} < \varpi < 6 \text{ kpc}$ ,  $0 \leq \varphi < 2\pi$  and  $0.1 \text{ kpc} < z < 1 \text{ kpc}$  (dashed curve),  $1.0 \text{ kpc} < z < 3.0 \text{ kpc}$  (dotted curve) and  $0.1 \text{ kpc} < z < 3.0 \text{ kpc}$  (solid curve), respectively. The unit of  $B_\varphi$  is  $\sqrt{\rho_b v_0^2} = 15 \mu \text{ G}$  in this model when  $\rho_b = 3 \times 10^{-25} \text{ g/cm}^3$ .



Fig. 20.— The dependence of azimuthally averaged magnetic energy on the azimuthal grid resolution and the size of the azimuthal simulation region. (a) Field amplification stage and (b) non-linear saturation stage. Magnetic energy is averaged in  $2 \text{ kpc} < \varpi < 5 \text{ kpc}$ , and  $0 \text{ kpc} < z < 1 \text{ kpc}$ . Azimuthal simulation region is  $2\pi$  for model III and  $\pi/2$  for model V, VI and VII. The azimuthal grid size is  $\pi/32$  for model III, and  $\pi/128, \pi/64$  and  $\pi/32$  for model V, VI and VII, respectively.



Fig. 21.— (a) Vertical distribution of azimuthal magnetic field  $B_\varphi$  at  $\varpi = 10 \text{ kpc}$  when  $t = 800t_0$  for model III, V, VI and VII. The dashed curve shows the initial profile of  $B_\varphi$ . (b) The time evolution of the rising magnetic flux for model III, V, VI and VII. The height of the wave front of the rising magnetic flux where  $B_\varphi = 0.003\sqrt{\rho_b v_0^2}$  is plotted.

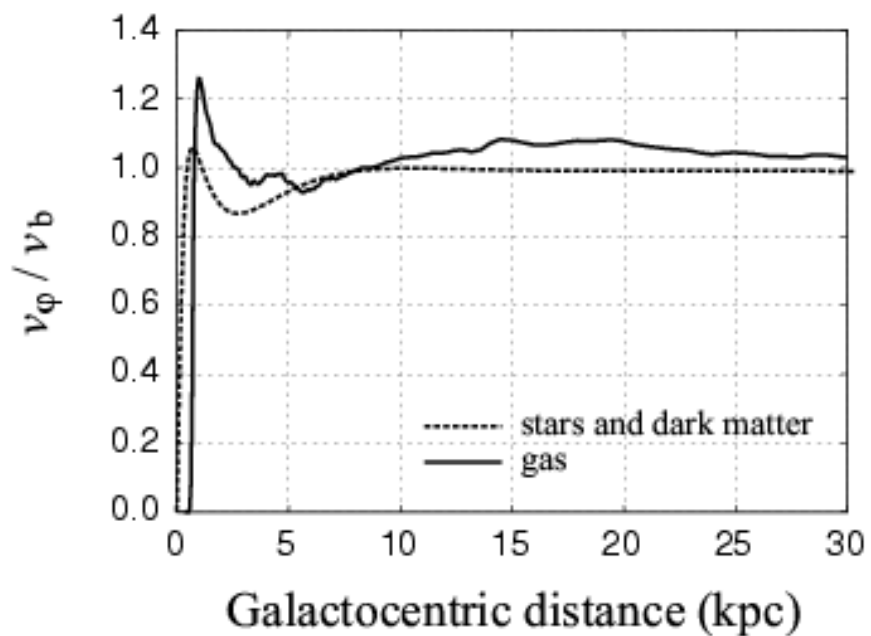


Fig. 22.— The rotation curve of stars and dark matter computed from the gravitational potential (dashed curve) and the rotation curve for gas (solid curve) obtained by simulations for model III at  $t = 3.8$  Gyr.